PHYSICAL REVIEW D **79,** 074506 (2009)

Electromagnetic form factor of the pion from twisted-mass lattice QCD at $N_f = 2$

R. Frezzotti,[1] V. Lubicz,[2] and S. Simula[3]

[1]*Dip. di Fisica, Università di Roma Tor Vergata and INFN, Sez. di Roma Tor Vergata, Via della Ricerca Scientifica, I-00133 Roma, Italy*

[2]*Dipartimento di Fisica, Università di Roma Tre and INFN, Sez. di Roma Tre, Via della Vasca Navale 84, I-00146 Roma, Italy*

[3]*Istituto Nazionale di Fisica Nucleare, Sezione di Roma Tre, Via della Vasca Navale 84, I-00146 Roma, Italy*

(Received 21 December 2008; published 15 April 2009)

We present a lattice calculation of the electromagnetic form factor of the pion obtained using the tree-level Symanzik improved gauge action with two flavors of dynamical twisted Wilson quarks. The simulated pion masses range approximately from 260 to 580 MeV, and the lattice box sizes are chosen in order to guarantee that $M_\pi L \gtrsim 4$. Accurate results for the form factor are obtained using all-to-all quark propagators evaluated by a stochastic procedure. The momentum dependence of the pion form factor is investigated up to values of the squared four-momentum transfer $Q^2 \simeq 0.8$ GeV^2 and, thanks to the use of twisted boundary conditions, down to $Q^2 \simeq 0.05$ GeV^2. Volume and discretization effects on the form factor appear to be within the statistical errors. Our results for the pion mass, decay constant and form factor are analyzed using (continuum) chiral perturbation theory at next-to-next-to-leading order. The extrapolated value of the pion charge radius is $\langle r^2 \rangle^{\rm phys} = 0.456 \pm 0.030_{\rm stat} \pm 0.024_{\rm syst}$ in nice agreement with the experimental result. The extrapolated values of the pion form factor agree very well with the experimental data up to $Q^2 \simeq 0.8$ GeV^2 within uncertainties which become competitive with the experimental errors for $Q^2 \gtrsim 0.3$ GeV^2. The relevant low-energy constants appearing in the chiral expansion of the pion form factor are extracted from our lattice data, which come essentially from a single lattice spacing, adding the experimental value of the pion scalar radius in the fitting procedure. Our findings are in nice agreement with the available results of chiral perturbation theory analyses of $\pi - \pi$ scattering data as well as with other analyses of our collaboration.

DOI: 10.1103/PhysRevD.79.074506 PACS numbers: 12.38.Gc, 12.39.Fe, 13.40.Gp, 14.40.Aq

I. INTRODUCTION

The investigation of the physical properties of the pion, which is the lightest bound state in quantum chromodynamics (QCD), can provide crucial information on the way low-energy dynamics is governed by the quark and gluon degrees of freedom. In this respect for spacelike values of the squared four-momentum transfer, $Q^2 \equiv -q^2 \geq 0$, the electromagnetic (e.m.) form factor of the pion, $F_\pi(Q^2)$, provides important insights on the distribution of its charged constituents, namely, valence and sea light quarks. At momentum transfer below the scale of chiral symmetry breaking ($Q^2 \lesssim 1$ GeV^2) the pion form factor represents therefore an important test of nonperturbative QCD.

The current experimental situation is as follows. For values of $Q^2 \lesssim 0.2$ GeV^2 the pion form factor has been determined quite precisely at CERN SPS [1] by measuring directly the scattering of high-energy pions off atomic electrons in a fixed target. At higher values of Q^2 the pion form factor is extracted from cross section measurements of the reaction $^1H(e, e'\pi^+)n$, that is from electron quasielastic scattering off virtual pions in a proton. The separation of the longitudinal and transverse response functions as well as the extrapolation of the observed scattering from virtual pions to the one corresponding to on-shell pions have to be carefully considered for estimating the systematic uncertainties. Using the electroproduction technique the pion form factor has been determined for Q^2 values in the range $0.4 \div 9.8$ GeV^2 at CEA/Cornell [2], for $Q^2 = 0.35$ and 0.70 GeV^2 at DESY [3,4] and, more recently, for Q^2 in the range $0.6 \div 1.6$ GeV^2 [5] and for $Q^2 = 1.60$, 2.15 and 2.45 GeV^2 [6] at the Thomas Jefferson National Acceleration Facility (JLab). A careful reanalysis of the systematic uncertainties for the data of Refs. [3–5] has been carried out in Refs. [7,8].

It is well known that at small values of Q^2 the pion form factor can be reproduced qualitatively by a simple monopole ansatz inspired by the vector meson dominance (VMD) model with the contribution from the lightest vector meson ($M_\rho \simeq 0.77$ GeV) only. This is not too surprising in view of the fact that in the timelike region the pion form factor is dominated by the ρ-meson resonance [9].

More interesting is the quark mass dependence of the pion form factor, which can be addressed by QCD simulations on the lattice and by chiral perturbation theory (ChPT). The latter, which is known at next-to-leading order (NLO) [10] and next-to-next-to-leading (NNLO) order [11] for the pion form factor, can be used as a guide to extrapolate the lattice results from the simulated pion masses down to the physical point, obtaining at the same time an estimate of the relevant low-energy constants (LECs) of the effective theory.

Initial studies of the pion form factor using lattice QCD date back to the late 1980s [12,13] giving strong support to

the vector-meson dominance hypothesis at low Q^2. Within the quenched approximation, which neglects the effects of the sea quarks, several lattice investigations have been carried out using Wilson [14], Sheikholeslami-Wohlert [15], twisted Wilson [16] and Ginsparg-Wilson [17] fermions. The effects of the quenched approximation might be limited because, thanks to charge-conjugation and isospin symmetries, the e.m. pion form factor receives no contribution from the so-called disconnected diagrams in which the vector current is attached directly to a nonvalence quark (see Ref. [13]). However there are effects from sea quarks which do not interact directly with the external current, and they can be taken into account only by performing unquenched gauge simulations.

There are few results for two flavors of dynamical fermions from the JLQCD [18] and QCDSF/UKQCD [19] Collaborations adopting Clover fermions and again from JLQCD [20] using overlap quarks. Finally only two studies with three flavors of dynamical quarks are available to date, namely, from Ref. [14], where domain-wall valence quarks and Asqtad sea quarks are mixed, and from Ref. [21], where the domain-wall formulation is used for both sea and valence quarks.

As far as the lattice results for the (squared) pion charge radius at the physical point are concerned, the present situation is a bit puzzling. Some collaborations [14,18] have found that their extrapolations underestimate significantly (up to $\simeq 30\%$) the well-known experimental value $\langle r^2\rangle^{\rm exp} = 0.452 \pm 0.011$ fm^2 [22], while other collaborations [19–21] have obtained values consistent with experiment within the errors.

The European Twisted-Mass (ETM) Collaboration has recently produced a large number of gauge configurations with two flavors of dynamical quarks [23–25] using the Wilson twisted-mass fermionic action [26] and the tree-level Symanzik improved (tlSym) gauge action [27]. In order to obtain (almost) automatic $\mathcal{O}(a)$ improvement the Wilson twisted-mass fermions have been tuned to maximal twists [28]. An intensive, systematic program of calculations of three-point correlation functions relevant for the determination of meson form factors both in the light and in the heavy sectors has then been started. Preliminary results, concerning the vector and scalar form factors of the pion, the Isgur-Wise universal function and the transition form factors relevant in $K_{\ell 3}$ and $D \to \pi(K)$ semileptonic decays have been presented in Ref. [29].

In this paper we concentrate on the e.m. form factor of the pion, and we present the results of several measurements performed with pion masses in the range from $\simeq 260$ MeV to $\simeq 580$ MeV, using six values of the quark mass at a lattice spacing of $\simeq 0.09$ fm and two values of the quark mass at a lattice spacing of $\simeq 0.07$ fm. The lattice box sizes are chosen in order to guarantee that $M_\pi L \gtrsim 4$ for minimizing as much as possible finite size effects. Thanks to the use of all-to-all propagators evaluated by the stochastic procedure of Ref. [30] (see also [24]) the statistical precision of the extracted form factor is quite impressive. The momentum dependence of the pion form factor is investigated up to values of the squared four-momentum transfer $Q^2 \simeq 0.8$ GeV^2 and, thanks to the use of twisted boundary conditions (BCs) [31,32], down to $Q^2 \simeq 0.05$ GeV^2. The Q^2-shape at the simulated pion masses is well reproduced by a single monopole ansatz with a pole mass lighter by $\approx 10\% \div 15\%$ than the lightest vector-meson mass. Volume and discretization effects on the form factor are estimated using few simulations at different volumes and lattice spacings, and they turn out to be within the statistical errors.

The extrapolation of our results for the pion mass, decay constant and form factor to the physical point is carried out using (continuum) ChPT at NNLO [11]. The extrapolated value of the (squared) pion charge radius is $\langle r^2\rangle^{\rm phys} = 0.456 \pm 0.030_{\rm stat} \pm 0.024_{\rm syst}$, in nice agreement with the experimental result $\langle r^2\rangle^{\rm exp} = 0.452 \pm 0.011$ fm^2 [22]. The extrapolated values of the pion form factor agree very well with the experimental data up to $Q^2 \simeq 0.8$ GeV^2 within uncertainties which become competitive with the experimental errors for $Q^2 \gtrsim 0.3$ GeV^2. The relevant low-energy constants (LECs) appearing in the chiral expansion of the pion form factor are extracted from our lattice data adding in the fitting procedure the experimental value of the pion scalar radius [11]. The latter helps to constrain one of the LECs ($\bar{\ell}_4$), which in turn is beneficial for reducing the uncertainties of the other LECs. We get: $\bar{\ell}_1 = -0.4 \pm 1.3 \pm 0.6$, $\bar{\ell}_2 = 4.3 \pm 1.1 \pm 0.4$, $\bar{\ell}_3 = 3.2 \pm 0.8 \pm 0.2$, $\bar{\ell}_4 = 4.4 \pm 0.2 \pm 0.1$, $\bar{\ell}_6 = 14.9 \pm 1.2 \pm 0.7$, where the first error is statistical and the second one systematic. Our findings are in nice agreement with the results of ChPT analyses of $\pi - \pi$ scattering data [33]. The values found for $\bar{\ell}_3$ and $\bar{\ell}_4$ agree very well both with earlier ETMC results from Refs. [23,24] and with the recent ETMC determination of Ref. [34]. This is quite reassuring because different kinds of systematic uncertainties may affect the two analyses: the present one being a NNLO analysis limited mainly to data from a single lattice spacing, and that of Ref. [34] having two values of the lattice spacing but limited mainly to NLO in ChPT.

The plan of the paper is as follows. In the next section we briefly discuss the implementation of twisted BCs for the quark fields. In Sec. III we present the calculation of two- and three-point correlation functions performed in the Breit reference frame, where the values of four-momentum transfer Q^2 are independent of the simulated pion mass. We also briefly show the stochastic procedure used for our unbiased estimate of the all-to-all propagators employed in this work.

In Sec. IV we first illustrate the very precise results obtained for the renormalization constant of the vector current, and then we compare them with other determinations. Our accurate results for the momentum dependence

of the pion form factor for the various simulated pion masses are presented, and both volume and discretization effects are investigated.

In Sec. V, using a single monopole ansatz to fit the momentum dependence of the form factor, the charge radius and the curvature are calculated at the simulated pion masses and analyzed both in terms of the ChPT expansion at NNLO from Ref. [11] and adopting a simple polynomial fit.

The mass and momentum dependencies of our lattice points for the pion form factor are analyzed in Sec. VI without any model assumption, but using only the functional forms dictated by ChPT at NNLO.

In Sec. VII the final values of the relevant LECs, including the estimate of the systematic errors, are presented, and it is shown that the extrapolated form factor at the physical point agrees very well with the experimental data in the whole range of values of Q^2 considered. Finally Sec. VIII is devoted to our conclusions.

II. LATTICE ALL-TO-ALL QUARK PROPAGATORS WITH TWISTED BOUNDARY CONDITIONS

In lattice QCD simulations the spatial components of the hadronic momenta p_j $(j = 1, 2, 3)$ are quantized. The specific quantized values depend on the choice of the BCs applied to the quark fields. The most common choice is the use of periodic BCs in the spatial directions

$$\psi(x + \hat{e}_j L) = \psi(x), \tag{1}$$

that leads to

$$p_j = n_j \frac{2\pi}{L}, \tag{2}$$

where the n_j's are integer numbers. Thus the smallest nonvanishing value of p_j is given by $2\pi/L$, which depends on the spatial size of the (cubic) lattice ($V = L^3$). For instance a current available lattice may have $L = 32a$, where a is the lattice spacing, and $a^{-1} \simeq 2.5$ GeV leading to $2\pi/L \simeq 0.5$ GeV. Such a value may represent a strong limitation of the kinematical regions accessible for the investigation of momentum-dependent quantities, like, e.g., form factors.

In Ref. [31] it was proposed to use twisted BCs for the quark fields

$$\tilde{\psi}(x + \hat{e}_j L) = e^{2\pi i \theta_j} \tilde{\psi}(x) \tag{3}$$

which allows to shift the quantized values of p_j by an arbitrary amount equal to $2\pi\theta_j/L$, namely

$$\tilde{p}_j = p_j + \theta_j \frac{2\pi}{L} = n_j \frac{2\pi}{L} + \theta_j \frac{2\pi}{L}. \tag{4}$$

The twisted BCs (3) can be shown [31] to be equivalent to the introduction of a U(1) background gauge field coupled to the baryon number and applied to quark fields satisfying usual periodic BCs (the Aharonov-Bohm effect). In Ref. [32] the twisted BCs were first implemented in a lattice QCD simulation of two-point correlation functions of pseudoscalar mesons. The energy-momentum dispersion relation was checked confirming that the momentum shift $2\pi\theta_j/L$ is a physical one. In Ref. [35] the twisted BCs were first applied to the calculation of the vector and scalar form factors relevant to the $K \to \pi$ semileptonic decay. It was shown that the momentum shift produced by the twisted BCs does not introduce any additional noise and easily allows to determine the form factors with good accuracy at quite small values of Q^2, which are not accessible when periodic BCs are considered.[1]

On the lattice, for a given flavor, the all-to-all quark propagator $S(x, y) \equiv \langle \psi(x) \bar{\psi}(y) \rangle$, where $\langle \ldots \rangle$ indicates the average over gauge field configurations weighted by the lattice QCD action, satisfies the following equation

$$\sum_z D(x, z) S(z, y) = \delta_{x,y} \tag{5}$$

where $D(x, z)$ is the Dirac operator whose explicit form depends on the choice of the lattice QCD action.[2] In what follows we work with the fermionic twisted-mass lattice QCD (tmLQCD) action with two flavors of mass-degenerate quarks given in Ref. [23], tuned at *maximal* twist in the way described in full details in Ref. [24]. Therefore, in the so-called physical basis the operator $D(x, z)$ is given explicitly by

$$D(x, z) = K(x, z) + i\gamma_5 \tau_3 W(x, z) + am\delta_{x,z}, \tag{6}$$

$$K(x, z) = \frac{1}{2} \sum_{\mu=1}^{4} \gamma_\mu \{\delta_{x,z-a\hat{\mu}} U_\mu(x) - \delta_{x,z+a\hat{\mu}} U_\mu^\dagger(z)\}, \tag{7}$$

$$W(x, z) = (4r + am_{\text{crit}})\delta_{x,z} - \frac{r}{2} \sum_{\mu=1}^{4} \{\delta_{x,z-a\hat{\mu}} U_\mu(x) + \delta_{x,z+a\hat{\mu}} U_\mu^\dagger(z)\}, \tag{8}$$

where $U_\mu(x)$ is the gauge link, m is the bare twisted quark mass, m_{crit} is the critical value of the untwisted quark mass (needed to achieve maximal twist), τ_3 is the third Pauli matrix acting in flavor space, and r is the Wilson parameter, which is set to $r = 1$ in our simulations.

[1] We mention that a new application of twisted BCs to the evaluation of the vector form factor at zero-momentum transfer has been proposed in Ref. [21].

[2] We omit in this section color and Dirac indices for simplicity.

We now want to consider the case in which a valence quark field satisfies the twisted BCs (3) in the spatial directions and is antiperiodic in time. This is at variance with what has been done in the production of the ETMC gauge configurations, which include two sea quarks with periodic BCs in space and antiperiodic ones in time [24]. However it has been recently shown [36] that for many physical quantities, which do not involve final state interactions (like, e.g., meson masses, decay constants, semileptonic form factors and e.m. transitions), the use of different BCs on valence and sea quarks produces finite-volume effects which remain exponentially small. In this way there is no need for producing new gauge configurations for each quark momentum, and this is quite relevant in the case of gauge configurations with dynamical fermions.

The corresponding quark propagator $\tilde{S}(x, y) \equiv \langle \tilde{\psi}(x)\bar{\tilde{\psi}}(y)\rangle$ still satisfies Eq. (5) with the same Dirac operator $D(x, z)$ but with different BCs:

$$\sum_z D(x, z)\tilde{S}(z, y) = \delta_{x,y}. \tag{9}$$

Technically in order to work always with fields satisfying periodic BCs in space and time we follow Refs. [31,32] by introducing a new quark field as

$$\psi_{\tilde{\theta}}(x) = e^{-2\pi i\tilde{\theta}\cdot x/L}\tilde{\psi}(x) \tag{10}$$

where the four-vector $\tilde{\theta}$ is given by $(L/2T, \vec{\theta})$. In such a way the new quark propagator $S^{\tilde{\theta}}(x, y) \equiv \langle \psi_{\tilde{\theta}}(x)\bar{\psi}_{\tilde{\theta}}(y)\rangle$ satisfies the equation

$$\sum_z D^{\tilde{\theta}}(x, z)S^{\tilde{\theta}}(z, y) = \delta_{x,y} \tag{11}$$

with a modified Dirac operator $D^{\tilde{\theta}}(x, z)$ but periodic BCs in both space and time. The new Dirac operator is related to Eq. (6) by a simple rephasing of the gauge links

$$U_\mu(x) \rightarrow U^{\tilde{\theta}}_\mu(x) \equiv e^{2\pi i a\tilde{\theta}_\mu/L}U_\mu(x). \tag{12}$$

In terms of $S^{\tilde{\theta}}(x, y)$, related to the quark fields $\psi_{\tilde{\theta}}(x)$ with periodic BCs, the all-to-all quark propagator $\tilde{S}(x, y)$, corresponding to the quark fields $\tilde{\psi}(x)$ with twisted BC's, is simply given by

$$\tilde{S}(x, y) = e^{2\pi i\tilde{\theta}\cdot(x-y)/L}S^{\tilde{\theta}}(x, y). \tag{13}$$

III. TWO- AND THREE-POINT CORRELATION FUNCTIONS

We are interested in the calculation of the vector form factor of a charged pion defined through the relation

$$\langle \pi^+(p')|\hat{V}_\mu(0)|\pi^+(p)\rangle = F_\pi(q^2)(p + p')_\mu, \tag{14}$$

where p (p') is the initial (final) pion four-momentum, $q^2 = (p - p')^2$ is the squared four-momentum transfer and $\hat{V}_\mu$ is a conserved e.m. current on the lattice. Splitting $\hat{V}_\mu$ into an isovector and an isoscalar part, it is easy to show that the matrix elements of the isoscalar component between pion states is vanishing in the continuum limit, thanks to charge conjugation and isospin symmetries.[3]

Thus, up to discretization effects we take $\hat{V}_\mu$ at a generic (Euclidean) space-time point $x = (t_x, \vec{x})$ in the following form

$$\hat{V}_\mu(x) = Z_V V_\mu(x), \tag{15}$$

$$V_\mu(x) = \frac{1}{2}[\bar{u}(x)\gamma_\mu u(x) - \bar{d}(x)\gamma_\mu d(x)] \tag{16}$$

with Z_V being the renormalization constant of the isovector part of the vector current at maximal twist (cf. Ref. [28]).

The insertion of the current (16) generates two types of Feynmann diagrams, the so-called connected and disconnected diagrams.[4] In the former the external current is attached to the valence quarks, whereas in the latter the current interacts with the sea quarks. However, in the continuum limit the vanishing of the pion-to-pion matrix element of the isoscalar current $(\bar{u}\gamma_\mu u + \bar{d}\gamma_\mu d)$ implies that the connected diagrams stemming from the u- and d-quark terms of the current (16) are equal in absolute value and opposite in sign, while their disconnected counterparts are vanishing for each quark flavor. Thus, in tmLQCD the disconnected diagrams for the e.m. pion form factor represent a pure discretization effect, which turns out to be of order $\mathcal{O}(a^2)$ (see later on). Therefore, up to discretization effects, it is enough to consider only the connected insertion of one single flavor of Eq. (16).

From Eq. (14) the pion form factor can be extracted from both the time and the spatial components of the vector current. However for reasons which will become clear during this section, we work in the Breit reference frame where $\vec{p}' = -\vec{p}$, so that the spatial components of the vector current are vanishing identically. Therefore we limit ourselves to consider the following two- and three-point correlation functions

$$C^\pi(t, \vec{p}) = \sum_{x,z}\langle O_\pi(x)O^\dagger_\pi(z)\rangle\delta_{t,t_x-t_z}e^{-i\vec{p}\cdot(\vec{x}-\vec{z})}, \tag{17}$$

$$C^{\pi\pi}_0(t, t', \vec{p}, \vec{p}') = \sum_{x,y,z}\langle O_\pi(y)V_0(x)O^\dagger_\pi(z)\rangle\delta_{t,t_x-t_z}\delta_{t',t_y-t_z} \cdot e^{-i\vec{p}\cdot(\vec{x}-\vec{z})+i\vec{p}'\cdot(\vec{x}-\vec{y})}, \tag{18}$$

where $V_0(x) = \bar{u}(x)\gamma_0 u(x)$ and $O^\dagger_\pi(z) = \bar{u}(z)\gamma_5 d(z)$ is the

[3]Note that in tmLQCD the charge-conjugation symmetry is preserved, while the isospin one is broken at finite lattice spacings.

[4]The terms "connected" and "disconnected" refer to fermionic lines only.

operator interpolating the π^+ mesons. Note that, since we want to use all-to-all propagators, in Eqs. (17) and (18) there is an additional sum over the space-time lattice volume, which helps in improving the signal quality with respect to the case of a fixed-point source ($z = 0$).

Using the completeness relation and taking t and $(t' - t)$ large enough, one gets

$$C^{\pi}(t, \vec{p}) \underset{t\to\infty}{\to} \frac{Z_\pi}{2E_\pi(\vec{p})} e^{-E_\pi(\vec{p})t}, \tag{19}$$

$$C_0^{\pi\pi}(t, t', \vec{p}, \vec{p}') \underset{(t'-t)\to\infty}{\overset{t\to\infty}{\to}} \frac{Z_\pi}{2E_\pi(\vec{p})2E_\pi(\vec{p}')} \frac{1}{Z_V} \times \langle \pi^+(p')|\hat{V}_0|\pi^+(p)\rangle e^{-E_\pi(\vec{p})t} \times e^{-E_\pi(\vec{p}')(t'-t)}, \tag{20}$$

where, up to discretization effects, $E_\pi(\vec{p}) = \sqrt{M_\pi^2 + |\vec{p}|^2}$ and $\sqrt{Z_\pi} = \langle 0|O_\pi(0)|\pi^+\rangle$ is independent on the meson momentum $\vec{p}$. Note that in tmLQCD at maximal twist the value of the coupling constant Z_π determines the pion decay constant f_π [28] without the need of the knowledge of any renormalization constant, namely

$$f_\pi = 2m \frac{\sqrt{Z_\pi}}{M_\pi^2}, \tag{21}$$

where m is the bare twisted quark mass.

Taking advantage of the choice of the Breit frame where $\vec{p}' = -\vec{p}$, it follows

$$\frac{C_0^{\pi\pi}(t, t', \vec{p}, -\vec{p})}{C^{\pi}(t', \vec{p})} \underset{(t'-t)\to\infty}{\overset{t\to\infty}{\to}} \frac{1}{Z_V} \frac{\langle \pi^+(p')|\hat{V}_0|\pi^+(p)\rangle}{2E_\pi(\vec{p})} = \frac{1}{Z_V} F_\pi(q^2), \tag{22}$$

where

$$q^2 \equiv [E_\pi(\vec{p}) - E_\pi(\vec{p}')]^2 - |\vec{p} - \vec{p}'|^2 \underset{\vec{p}'=-\vec{p}}{\to} -4|\vec{p}|^2 \tag{23}$$

is independent of the simulated pion mass.

The vector renormalization constant can be obtained from Eq. (22) by using the absolute normalization of the pion form factor at $q^2 = 0$, namely $F_\pi(q^2 = 0) = 1$, which implies

$$Z_V \underset{(t'-t)\to\infty}{\overset{t\to\infty}{\to}} \frac{C^{\pi}(t', \vec{0})}{C_0^{\pi\pi}(t, t', \vec{0}, \vec{0})}. \tag{24}$$

Combining Eqs. (22) and (24) one gets

$$R_0(t, t'; q^2) \equiv \frac{C_0^{\pi\pi}(t, t', \vec{p}, -\vec{p})}{C_0^{\pi\pi}(t, t', \vec{0}, \vec{0})} \frac{C^{\pi}(t', \vec{0})}{C^{\pi}(t', \vec{p})} \underset{(t'-t)\to\infty}{\overset{t\to\infty}{\to}} F_\pi(q^2) \tag{25}$$

which means that the pion form factor can be obtained directly from the plateau of the double ratio given by the left-hand side of Eq. (25) at large time distances. Note that in this way the normalization condition $F_\pi(q^2 = 0) = 1$ is fulfilled at all quark masses, lattice volumes and spacings.

The (mass-dependent) renormalization constant Z_V can be obtained alternatively using the three-point correlation function calculated in a frame in which the initial and final pions have the same momentum $\vec{p}$, i.e., from the plateau of the ratio $C^{\pi}(t', \vec{p})/C_0^{\pi\pi}(t, t', \vec{p}, \vec{p})$ at large time distances. In this way the pion form factor can be extracted from the plateau of a ratio of three-point correlation functions only, i.e., from $C_0^{\pi\pi}(t, t', \vec{p}, -\vec{p})/C_0^{\pi\pi}(t, t', \vec{p}, \vec{p})$. Such an alternative approach has been tested in Ref. [21] and shown to have a statistical precision similar to the one based on Eq. (25).

In terms of the all-to-all quark propagators $S^{u(d)}(x, z)$, where the flavor labels u and d correspond to $\tau_3 = \pm 1$ in Eq. (6), the two-point function $C^{\pi}(t, \vec{p})$ of the charged pion becomes

$$C^{\pi}(t, \vec{p}) = \sum_{x,z} \langle \mathrm{Tr}[S_u(x, z)\gamma_5 S_d(z, x)\gamma_5]\rangle \delta_{t,t_x-t_z} e^{-i\vec{p}\cdot(\vec{x}-\vec{z})}. \tag{26}$$

For the tmLQCD action the γ_5-hermiticity property

$$S_d(z, x) = \gamma_5 S_u^{\dagger}(x, z)\gamma_5 \tag{27}$$

holds with the dagger operator acting in the (suppressed) color and Dirac spaces.

As for the three-point correlation function $C_0^{\pi\pi}(t_x, t_y, \vec{p}, -\vec{p})$, according to the discussion on the disconnected diagrams made before Eq. (18), up to discretization effects one gets

$$C_0^{\pi\pi}(t, t', \vec{p}, -\vec{p}) = \sum_{x,z} \langle \mathrm{Tr}[S_u(x, z)\gamma_5 \bar{\Sigma}_{du}(z, x; t'; -\vec{p})\gamma_0]\rangle \times \cdot \delta_{t,t_x-t_z} e^{-2i\vec{p}\cdot(\vec{x}-\vec{z})}, \tag{28}$$

where $\bar{\Sigma}_{du}(z, x; t'; -\vec{p}) = \gamma_5[\Sigma_{du}(x, z; t'; -\vec{p})]^{\dagger}\gamma_5$ and

$$\Sigma_{du}(x, z; t'; \vec{p}) = \sum_y S_d(x, y)\gamma_5 S_u(y, z) e^{-i\vec{p}\cdot(\vec{z}-\vec{y})} \delta_{t',t_y-t_z}. \tag{29}$$

The *sequential* propagator $\Sigma_{du}(x, z; t'; \vec{p})$ satisfies the equation

$$\sum_y D_d(x, y)\Sigma_{du}(y, z; t'; \vec{p}) = \gamma_5 S_u(x, z)\delta_{t',t_x-t_z} e^{i\vec{p}\cdot(\vec{x}-\vec{z})}. \tag{30}$$

As it has been shown in Ref. [28], the calculation of correlation functions of parity symmetric operators is automatically $\mathcal{O}(a)$ improved at maximal twist. Thus for nonvanishing values of the spatial momenta the $\mathcal{O}(a)$ terms can be eliminated by appropriate averaging of the correlation functions over initial and final momenta of opposite sign. Using the symmetry of correlation functions under the spatial inversion and the simultaneous exchange of u

and d quarks (which is fulfilled only after gauge averaging at maximal twist in the physical basis) as well as the charge-conjugation symmetry and the γ_5-hermiticity property, one gets that: i) the correlators (26) and (28) are real, and ii) $C^{\pi}(t', \vec{p}) = C^{\pi}(t', -\vec{p})$ and $C_0^{\pi\pi}(t, t', \vec{p}, -\vec{p}) = C_0^{\pi\pi}(t, t', -\vec{p}, \vec{p})$. Thus discretization effects in both $C^{\pi}(t', \vec{p})$ and $C_0^{\pi\pi}(t, t', \vec{p}, -\vec{p})$ start automatically at order $\mathcal{O}(a^2)$.[5]

Let us now consider the case of quark fields with twisted BCs. Equations (26)–(30) hold as well by simply replacing the propagators S and Σ with the corresponding twisted ones, $\tilde{S}$ and $\tilde{\Sigma}$, and by taking into account the change of the quantized momenta, namely $p_j \to \tilde{p}_j$ [see Eq. (4)]. The two- and three-point correlators can be expressed in terms of quark propagators satisfying periodic BCs, e.g., in terms of $S^{\tilde{\theta}}$ [see Eq. (13)]. We now write down the explicit formulae for sake of completeness.

In order to work in the Breit frame we consider three choices of the twisting four-vector $\tilde{\theta}$, namely $\tilde{\theta} = \tilde{\theta}_{\pm} = (L/2T, \pm\vec{\theta})$ and $\tilde{\theta} = \tilde{\theta}_0 = (L/2T, \vec{0})$ for various values of $\vec{\theta}$. Writing $\vec{p}$ in the generic form $\vec{p} = 2\pi\vec{\theta}/L$, we get

$$C^{\pi}\left(t, \frac{2\pi}{L}\vec{\theta}\right) = \sum_{x,z} \langle \mathrm{Tr}[S_u^{\tilde{\theta}_+}(x, z)\gamma_5 S_d^{\tilde{\theta}_0}(z, x)\gamma_5]\rangle \delta_{t,t_x-t_z}, \tag{31}$$

$$C_0^{\pi\pi}\left(t, t', \frac{2\pi}{L}\vec{\theta}, -\frac{2\pi}{L}\vec{\theta}\right) = \sum_{x,z} \langle \mathrm{Tr}[S_u^{\tilde{\theta}_+}(x, z)\gamma_5 \bar{\Sigma}_{du}^{\tilde{\theta}_0,\tilde{\theta}_-}(z, x; t')\gamma_0]\rangle \delta_{t,t_x-t_z}, \tag{32}$$

where thanks to the γ_5-hermiticity property one has

$$\bar{\Sigma}_{du}^{\tilde{\theta}_0,\tilde{\theta}_-}(z, x; t') = \gamma_5 [\Sigma_{du}^{\tilde{\theta}_-,\tilde{\theta}_0}]^{\dagger}(x, z; t')\gamma_5 \tag{33}$$

and the sequential propagator $\Sigma_{du}^{\tilde{\theta}_-,\tilde{\theta}_0}(x, z; t')$ satisfies the modified Dirac equation

$$\sum_y D_d^{\tilde{\theta}_-}(x, y)\Sigma_{du}^{\tilde{\theta}_-,\tilde{\theta}_0}(y, z; t') = \gamma_5 S_u^{\tilde{\theta}_0}(x, z)\delta_{t',t_x-t_z}. \tag{34}$$

Note that, because of Eq. (13), no exponential factors appear in the right-hand side of Eqs. (31)–(34), and the dependence on the vector $\vec{\theta}$ is totally embedded in the twisted quark propagators $S^{\tilde{\theta}_+}$ and $\Sigma^{\tilde{\theta}_-,\tilde{\theta}_0}$.

A. Stochastic procedures

The next point to be addressed is the evaluation of the all-to-all propagator $S^{\tilde{\theta}}(x, z)$, which is the solution of the modified Dirac equation (11). Restoring color and spin indices, denoted by Latin and Greek letters, respectively, one has

$$\sum_y [D^{\tilde{\theta}}(x, y)]_{\alpha\beta}^{ab} [S^{\tilde{\theta}}(y, z)]_{\beta\gamma}^{bc} = \delta_{x,z}\delta_{a,c}\delta_{\alpha,\gamma}. \tag{35}$$

The computation of exact all-to-all quark propagators is a formidable task well beyond present computational capabilities, because it involves a huge number of inversions of the Dirac equation for all possible locations of the source in space and time. Consequently most of the lattice computations of connected two- and three-point correlation functions are until now carried out using the point-to-all propagator by fixing the source at some space-time point, referred to as the origin. To get the expressions of our two- and three-point correlators in terms of point-to-all propagators it is enough to limit the sum over the variable z to $z = 0$ everywhere in Eqs. (31)–(34). The basic advantage of the all-to-all propagator with respect to the point-to-all one relies on the fact that the former contains all the information on the gauge configuration, which in turn means that the calculation of two- and three-point functions using all-to-all propagators is expected to have much less gauge noise.

An efficient way to estimate the all-to-all propagator is based on stochastic techniques with the help of variance reduction methods to better separate the signal from the noise (see Ref. [37] and references therein). In recent years new stochastic methods have been developed, like the dilution method of Ref. [38] and the so-called "one-end-trick" of Ref. [30]. The latter, already applied by the ETM Collaboration to the calculation of neutral meson masses (see Refs. [24,39]), allows to achieve a great reduction of the noise-to-signal ratio, and it will be applied in this work to the calculation of three-point correlation functions (see also Refs. [29,40]).

The starting point of all stochastic approaches is to consider random sources $\eta_r^a(x)$, which, for reasons that will become clear later on, we take independent of both the spin variable and the twisting vector $\tilde{\theta}$ (i.e., of the quark momentum). The index r ($r = 1, \ldots N$) enumerates the generated random sources, which must satisfy the following constraint:

$$\lim_{N\to\infty} \frac{1}{N} \sum_{r=1}^{N} \eta_r^a(x)[\eta_r^b(y)]^* = \delta_{a,b}\delta_{x,y}. \tag{36}$$

In this work we adopt for the sources a random choice of ± 1 values. Then one introduces the "ϕ-propagator"

$$[\phi_r^{\tilde{\theta}}(x)]_{\alpha\beta}^a = \sum_y [S^{\tilde{\theta}}(x, y)]_{\alpha\beta}^{ab} \eta_r^b(y), \tag{37}$$

which is solution of the equation

$$\sum_y [D^{\tilde{\theta}}(x, y)]_{\alpha\beta}^{ab} [\phi_r^{\tilde{\theta}}(y)]_{\beta\gamma}^b = \eta_r^a(x)\delta_{\alpha,\gamma}, \tag{38}$$

where the sum over repeated color or spin indices is under-

[5]This result holds as well in all reference frames and it explains the findings shown in Fig. 12 of Ref. [16], where the correlation functions with opposite momenta have been calculated explicitly and found to be identical within statistical errors.

stood. As explained in detail in Ref. [24], the quantity $(1/N)\sum_{r=1}^{N}[\phi_r^{\tilde{\theta}}(x)]_{\alpha\beta}^{a}[\eta_r^{b}(y)]^*$ is an unbiased estimator of the all-to-all propagator $[S^{\tilde{\theta}}(x,y)]_{\alpha\beta}^{ab}$. However, while the signal is of order $\mathcal{O}(1)$, the noise is of the order $\sqrt{V/N}$ (where V is the space-time volume) and therefore a huge number of random sources and inversions of Eq. (38) would be required.

The "one-end-trick" is based on the observation that the product of two "ϕ-propagators" is an unbiased estimator of the product of two all-to-all propagators summed over the intermediate space-time points. In this case, however, the signal is of order V, while the noise is of order $V/\sqrt{N}$, so that it is even sufficient to employ one random source per gauge configuration, as we do in this work.

Choosing the random source $\eta_a^r(x)$ to be nonvanishing only for a randomly chosen time slice, located at t_r,[6] the two-point correlation function (31) can be estimated as

$$C^{\pi}\left(t,\frac{2\pi}{L}\vec{\theta}\right)=\sum_{\vec{x},t_x}\langle[\phi_{u,r}^{\tilde{\theta}_+}(\vec{x},t_x)]_{\alpha\beta}^{a}\{[\phi_{u,r}^{\tilde{\theta}_0}(\vec{x},t_x)]_{\beta\alpha}^{a}\}^*\delta_{t,t_x-t_r}\rangle \tag{39}$$

where we notice that the two ϕ's have the same flavor. Looking at the above equation the ϕ-propagator $[\phi_r^{\tilde{\theta}}(x)]_{\alpha\beta}^{a}$ plays a role quite similar to the one of the point-to-all propagator $[S^{\tilde{\theta}}(x,0)]_{\alpha\beta}^{ab}$ with only one color index being the other one carried by the random source. This means that the time needed for the calculation of the ϕ-propagator is $1/3$ of that required for the point-to-all propagator. Note also that both $\phi_r^{\tilde{\theta}_+}(x)$ and $\phi_r^{\tilde{\theta}_0}(x)$ are solutions of Eq. (38) with the same random source $\eta_r(x)$. This is essential to properly get the right-hand side of Eq. (39). Moreover the independence of the random source from spin indices allows to evaluate two-point correlation functions with interpolating fields of the form $(\bar{q}\Gamma q')$ for any Dirac matrix Γ.

The stochastic estimate of the three-point correlation function (32) requires the introduction of the sequential "Φ-propagator"

$$[\Phi_{du,r}^{\tilde{\theta}_-,\tilde{\theta}_0}(x;t')]_{\alpha\beta}^{a}=\sum_{y}[\Sigma_{du,r}^{\tilde{\theta}_-,\tilde{\theta}_0}(x,y;t')]_{\alpha\beta}^{ab}\eta_r^{b}(y), \tag{40}$$

which is a solution of the equation

$$\sum_{y}[D_d^{\tilde{\theta}_-}(x,y)]_{\alpha\beta}^{ab}[\Phi_{du,r}^{\tilde{\theta}_-,\tilde{\theta}_0}(y;t')]_{\beta\rho}^{b}=[\gamma_5]_{\alpha\gamma}[\phi_{u,r}^{\tilde{\theta}_0}(x)]_{\gamma\rho}^{a}\delta_{t',t_x-t_r}. \tag{41}$$

One gets

$$C_0^{\pi\pi}\left(t,t',\frac{2\pi}{L}\vec{\theta},-\frac{2\pi}{L}\vec{\theta}\right)=\sum_{\vec{x},t_x}\langle[\phi_{u,r}^{\tilde{\theta}_+}(\vec{x},t_x)]_{\alpha\beta}^{a}\{[\Phi_{du,r}^{\tilde{\theta}_-,\tilde{\theta}_0}(\vec{x},t_x;t')]_{\beta\gamma}^{a}\}^*\cdot[\gamma_5\gamma_0]_{\gamma\alpha}\delta_{t,t_x-t_r}\rangle. \tag{42}$$

Note that: i) the quark propagators required in Eqs. (39) and (42) are those of one single flavor, while the other quark flavor appears only in the modified Dirac operator of Eq. (41), and ii) for each value of the quark momentum injected via the twisted BCs a new inversion of the Dirac operator is required.

IV. THE CHARGED PION FORM FACTOR

As already mentioned in the Introduction, the ETM Collaboration has started an intensive, systematic program of calculations of three-point correlation functions relevant for the determination of meson form factors at low, intermediate and heavy quark masses. In this work we concentrate on the results obtained for the vector form factor of the pion.

In Table I we collect the simulation setup for all the runs carried out at $\beta = 3.9$ and for the two runs performed at a finer lattice spacing ($\beta = 4.05$). Approximate values of the (charged) pion mass M_π in physical units as well as of the quantity $M_\pi L$, which governs finite-volume effects in the so-called p-regime of ChPT, are reported for each run.

The gauge configurations used for the measurements are selected from the trajectories produced by the ETM Collaboration (see Refs. [23–25]) at various values of the sea (bare) quark mass, $am_{\rm sea}$. We have chosen 1 configuration out of at least 20 (equilibrated) trajectories in all cases except for the run at the lightest pion mass (1 out of 10).

Volume effects can be checked through the runs R_{2a} and R_{2b} (see later Sec. IV D), while lattice artifacts can be studied by means of the runs R_{2b} and R_{2c} at a pion mass around 300 MeV and of the runs R_{5a} and R_{5b} for $M_\pi \simeq 480$ MeV (see later Sec. IV E).

In this work at each value of the (bare) quark mass, $am = am_{\rm sea}$, the statistical errors are evaluated with the jackknife procedure, while a bootstrap sampling will be applied in order to combine the jackknives for different quark masses (see later Sec. V).

A. Vector renormalization constant Z_V

In tmLQCD tuned at maximal twist the constant Z_V renormalizes both the isovector part of the (local) e.m. current [see Eq. (16)] and the isovector off-diagonal components of the (local) axial current, e.g., $A_\mu(x) = \bar{d}(x)\gamma_\mu\gamma_5 u(x)$. Therefore the renormalization constant Z_V can be calculated in two ways. The first one is from Eq. (24), which makes use of two- and three-point correlation functions and is equivalent to fix the absolute nor-

[6] The random choice of the time slice at t_r is mainly motivated by the reduction of autocorrelations observed for fermionic quantities using the ETM gauge ensembles (see Ref. [24]).

TABLE I. Setup of the lattice simulations for the various runs considered in this work.

β	a (fm)	Run	Refs. [24,25]	$am_{\rm sea}$	$V \cdot T/a^4$	M_π (MeV)	$M_\pi L$	No. gauge config.
3.9	$\simeq 0.09$	R_1	B_7	0.0030	$32^3 \cdot 64$	$\simeq 260$	$\simeq 3.7$	240
		R_{2a}	B_6	0.0040	$32^3 \cdot 64$	$\simeq 300$	$\simeq 4.2$	240
		R_{2b}	$B_{1a,b,c}$	0.0040	$24^3 \cdot 48$	$\simeq 300$	$\simeq 3.2$	480
		R_3	B_2	0.0064	$24^3 \cdot 48$	$\simeq 380$	$\simeq 4.0$	240
		R_4	$B_{3a,b}$	0.0085	$24^3 \cdot 48$	$\simeq 440$	$\simeq 4.7$	240
		R_{5a}	B_4	0.0100	$24^3 \cdot 48$	$\simeq 480$	$\simeq 5.1$	240
		R_6	$B_{5a,b}$	0.0150	$24^3 \cdot 48$	$\simeq 580$	$\simeq 6.1$	240
4.05	$\simeq 0.07$	R_{2c}	C_1	0.0030	$32^3 \cdot 64$	$\simeq 300$	$\simeq 3.4$	240
		R_{5b}	C_3	0.0080	$32^3 \cdot 64$	$\simeq 480$	$\simeq 5.4$	240

malization of the pion form factor, $F_\pi(0) = 1$. The second way is from the nonsinglet axial Ward Identity (WI), which, up to discretization effects, in tmLQCD at maximal twist reads as [28]

$$Z_V \partial_\mu A_\mu(x) = 2amP_5(x) \tag{43}$$

where am is the bare quark mass and $P_5(x) = \bar{d}(x)\gamma_5 u(x)$ is the bare pseudoscalar density. The presence of bare operators in the right-hand side of Eq. (43) is due to the fact that at maximal twist the mass renormalization constant is equal to the inverse of the pseudoscalar renormalization constant, i.e., $Z_m = Z_P^{-1}$. At zero momentum it follows

$$Z_V = 2am \frac{C^\pi(t, \vec{0})}{\partial_t A^\pi(t, \vec{0})} \tag{44}$$

with $A^\pi(t, \vec{0}) = \sum_{x,z} \langle A_0(x) P_5(z) \rangle \delta_{t,t_x - t_z}$.

The results obtained for the ratio given by the right-hand side of Eq. (24), evaluated for all the runs at $\beta = 3.9$ and $V \cdot T = 24^3 \cdot 48a^4$, are shown in Fig. 1(a). The time distance t' between the time slices of the source and the sink is fixed at $t' = T/2$, so that the three-point correlation function (18) becomes antisymmetric with respect to $t = T/2$, and it can be appropriately averaged to reduce the statistical fluctuations. Moreover for finite time extension T the two-point correlation function $C^\pi(t, \vec{p})$ is symmetric with respect to $t = T/2$, so that a second exponential $e^{-E_\pi(\vec{p})(T-t)}$ appears in Eq. (19) and a factor $1/2$ has to be applied to the right-hand side of Eq. (24).

From the plateau region denoted by the vertical dotted lines in Fig. 1(a) an estimate of the renormalization constant Z_V can be obtained at each value of the bare quark mass. The results are reported in Fig. 1(b) and compared with the corresponding results obtained from the WI using Eq. (44) (see Ref. [41]). Both methods exhibit an extremely high statistical precision of the order of 0.3%.

The quark mass dependence visible in Fig. 1(b) is a pure discretization effect and is different between the two methods. It appears to be linear in both cases, which is not in contradiction with the $\mathcal{O}(a)$ improvement, since terms

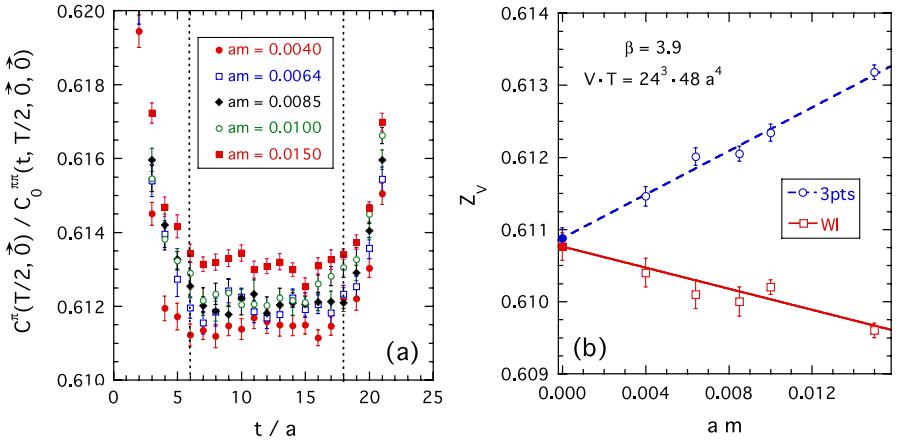

FIG. 1 (color online). (a) Ratio of two-point and three-point correlation functions given by the right-hand side of Eq. (24), evaluated for $t' = T/2$ at $\beta = 3.9$ and $V \cdot T = 24^3 \cdot 48a^4$, versus the (Euclidean) time t in lattice units. (b) The vector renormalization constant Z_V as obtained at different values of the bare quark mass in lattice units. Open dots correspond to the values extracted from the plateau region denoted by the vertical dotted lines in (a). Open squares are the results obtained from the WI using Eq. (44) in Ref. [41]. The solid and dashed lines are simple linear interpolations of the lattice points and the full markers denote the corresponding values at the chiral point.

proportional to $a^2 m \Lambda_{\rm QCD}$ may be dominant with respect to terms proportional to $a^2 m^2$.

The extrapolations to the chiral limit should therefore coincide, providing the value of the renormalization constant Z_V, which is indeed defined in such a limit. From Fig. 1(b) it can be seen that the values obtained by a simple linear fit at the chiral point coincide nicely within quite small statistical errors, namely $Z_V = 0.61088(14)$ from Eq. (24) and $Z_V = 0.61076(19)$ from the WI [Eq. (44)].

B. Momentum dependence of the two-point correlation function

The two-point correlation function (39) has been calculated for various values of the twisting angle $\vec{\theta}$ chosen always in the symmetric form $\vec{\theta} = (\theta, \theta, \theta)$ with $\theta = \{0.0, 0.11, 0.19, 0.27, 0.35, 0.44\}$. The time behavior of the effective mass (or logarithmic slope) $aM_{\rm eff}(t)$, defined as

$$aM_{\rm eff}(t) \equiv \log\left[\frac{C^\pi(t, 2\pi\vec{\theta}/L)}{C^\pi(t+a, 2\pi\vec{\theta}/L)}\right], \qquad (45)$$

is shown in Fig. 2 for two (representative) values of M_π at $\beta = 3.9$ and $V \cdot T = 24^3 \cdot 48 a^4$.

It can be seen that the statistical precision is remarkably high and it allows to extract quite precisely the energy $E_\pi(\vec{p})$ [see Eq. (19)] corresponding to the pion ground state, which starts to dominate from $t/a = 10$.

The values obtained for the pion energy $E_\pi(\vec{p})$ are shown in Fig. 3 as a function of the pion momentum given

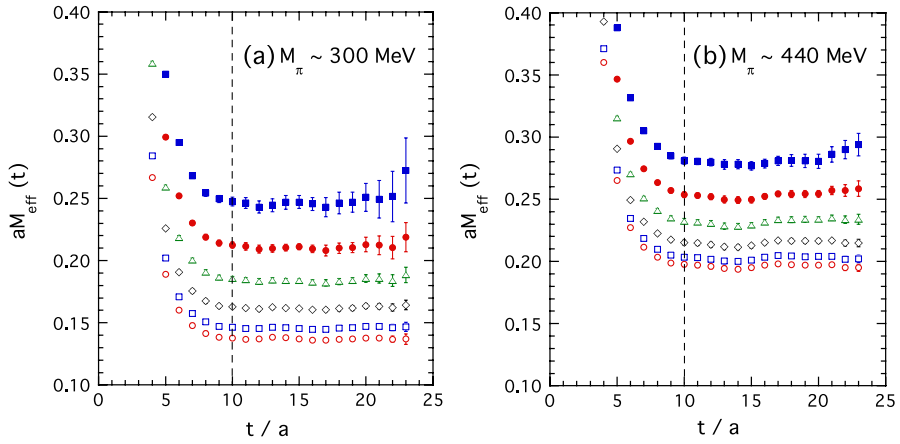

FIG. 2 (color online). Effective mass of the pion (45) versus the (Euclidean) time distance in lattice units for $M_\pi \simeq 300$ MeV (a) and $M_\pi \simeq 440$ MeV (b) at $\beta = 3.9$ and $V \cdot T = 24^3 \cdot 48 a^4$. The twisting angle $\vec{\theta}$ is chosen in the symmetric form $\vec{\theta} = (\theta, \theta, \theta)$. The dots, squares, diamonds, triangles, the full dots and the full squares correspond to $\theta = \{0.0, 0.11, 0.19, 0.27, 0.35, 0.44\}$, respectively. The dashed vertical line is drawn at $t/a = 10$, where the ground state starts to dominate.

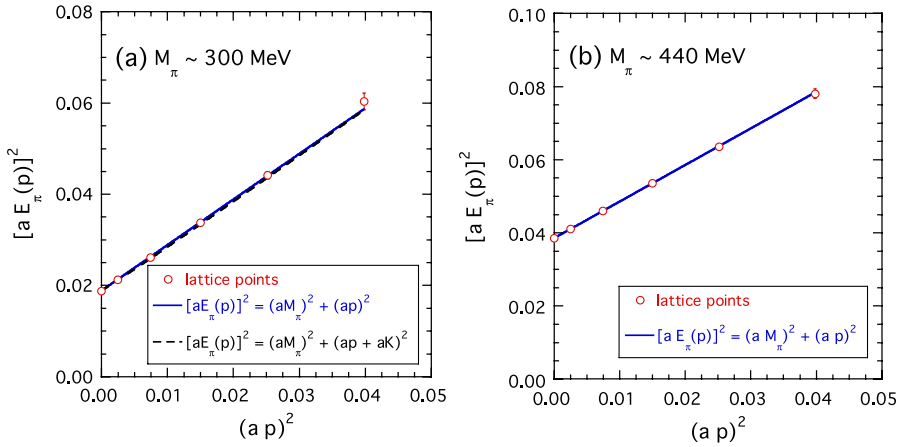

FIG. 3 (color online). Squared pion energy $E_\pi^2(\vec{p})$ in lattice units, obtained from the time plateaux of the effective mass shown in Fig. 2 (by choosing the time interval $10 \le t/a \le 21$), versus the squared pion momentum $p^2 \equiv 3(2\pi\theta/L)^2$ in lattice units, for $M_\pi \simeq 300$ MeV (a) and $M_\pi \simeq 440$ MeV (b) at $\beta = 3.9$ and $V \cdot T = 24^3 \cdot 48 a^4$. The solid line is the continuumlike dispersion relation $E_\pi^2(\vec{p}) = M_\pi^2(L) + |\vec{p}|^2$, while the dashed line in (a), which can be hardly distinguished from the solid one, represents the modified dispersion relation (46) predicted by partially twisted and partially quenched ChPT at NLO elaborated in Ref. [42].

by $\vec{p} \equiv 2\pi\vec{\theta}/L$, always at $\beta = 3.9$ and $V \cdot T = 24^3 \cdot 48a^4$. The lattice points appear to be in remarkable agreement with the continuumlike dispersion relation $E_\pi(\vec{p}) = \sqrt{M_\pi^2(L) + |\vec{p}|^2}$, where $M_\pi(L)$ is the charged pion mass at finite volume. We have also checked that, assuming the continuum dispersion relation for the energy, all the two-point correlation functions of moving pions can be simultaneously fitted very well together with the one at rest using a single momentum-independent matrix element Z_π [see Eq. (19)]. These findings clearly indicate that, at least for $t/a \geq 10$, where the ground state dominates, and for the pion momenta considered in this study, the discretization effects on the two-point correlation functions $C^\pi(t, 2\pi\vec{\theta}/L)$ are almost the same as those affecting the correlator at rest $C^\pi(t, \vec{0})$, which were investigated in Ref. [25] and found to be small.

The use of twisted BCs is expected to produce finite-volume corrections to the continuumlike dispersion relation. Such corrections have been investigated in Ref. [42] using partially quenched ChPT at NLO. In the case of charged pion and adopting twisted BCs for one flavor only, the pion momentum $\vec{p}$ acquires an additive correction term $\vec{K}$, namely

$$E_\pi^2(\vec{p}) = M_\pi^2(L) + (\vec{p} + \vec{K})^2 \tag{46}$$

where the components of the vector $\vec{K}$ are given by ($i \neq j \neq k$)

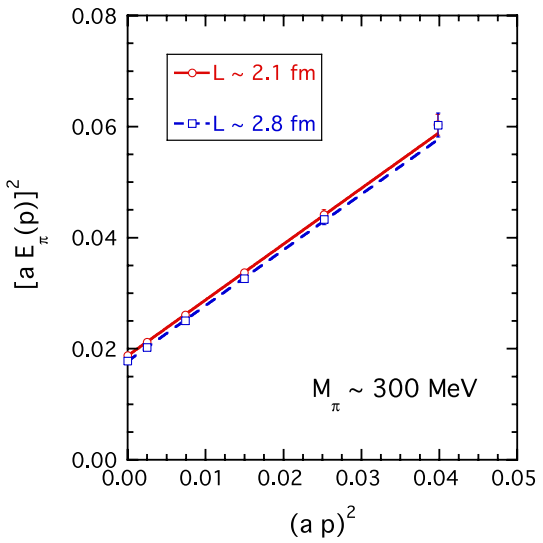

FIG. 4 (color online). Squared pion energy $E_\pi^2(\vec{p})$ in lattice units at $M_\pi \simeq 300$ MeV and $\beta = 3.9$ for the two runs R_{2a} and R_{2b}, performed at the volumes $V \cdot T = 24^3 \cdot 48a^4$ (dots) and $V \cdot T = 32^3 \cdot 64a^4$ (squares). The values of the twisting angle θ are chosen in such a way that θ/L has the same values in the two runs. The solid and dashed lines represent the continuumlike dispersion relation $E_\pi^2(\vec{p}) = M_\pi^2(L) + |\vec{p}|^2$.

$$K_i = -\frac{1}{\sqrt{\pi} f_\pi^2 L^3} \int_0^\infty d\tau \frac{1}{\sqrt{\tau}} e^{-\tau(M_\pi L/2\pi)^2} \bar{\Theta}(\tau, \theta_i)\Theta(\tau, \theta_j) \times \Theta(\tau, \theta_k) \tag{47}$$

with $\Theta(\tau, \theta)$ and $\bar{\Theta}(\tau, \theta)$ being the elliptic Jacobi function and its derivative. Explicitly one has $\Theta(\tau, \theta) \equiv \sum_{n=-\infty}^{\infty} e^{-\tau(n+\theta)^2}$ and $\bar{\Theta}(\tau, \theta) = \sum_{n=-\infty}^{\infty}(n + \theta)e^{-\tau(n+\theta)^2}$.

We have evaluated Eq. (47) for the run R_{2b}, which has the smallest value of $M_\pi L$ (see Table I). The results are reported in Fig. 3(a) (dashed line), and they clearly indicate the smallness of the volume corrections to the pion momentum and therefore to the continuum dispersion relation expected at NLO. Thus finite size effects may be limited mainly to the pion mass and thus expected to be small (see Refs. [23,24]). This is confirmed by the lattice results shown in Fig. 4, where the pion energies obtained in case of the runs R_{2a} and R_{2b}, which differ only for the lattice size, are compared.

C. Momentum dependence of the pion form factor

The advantage of calculating the pion form factor using all-to-all propagators, evaluated by the one-end-trick procedure with twisted BCs, with respect to the standard procedure based on point-to-all propagators with fixed sources and (spatially) periodic BCs, is illustrated in Fig. 5. From the run R_{2b} we choose a different number of

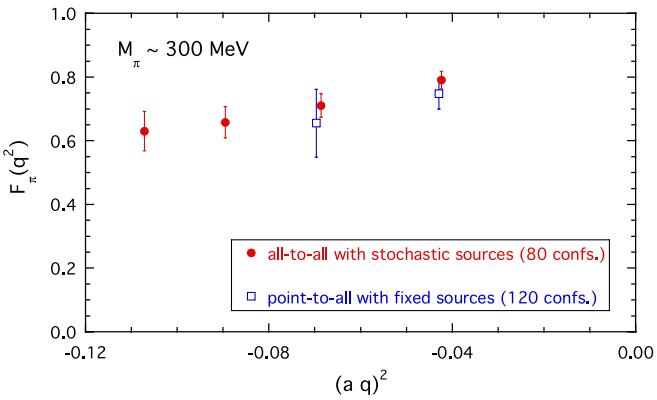

FIG. 5 (color online). Pion form factor $F_\pi(q^2)$ versus q^2 in lattice units for a simulated pion mass of $\simeq 300$ MeV. The full dots are the results obtained using twisted BCs in the Breit frame and the one-end-trick procedure for calculating the all-to-all propagators for an ensemble of 80 gauge configurations taken from the run R_{2b}. The open squares correspond to the results of the standard procedure based on point-to-all propagators with fixed sources for 120 gauge configurations of the run R_{2b}. In this case spatially periodic BCs are applied in the frame where the final pion is at rest ($\vec{p}' = 0$) and the momentum of the initial pion is given by $\vec{p} = 2\pi/L\{(1, 0, 0), (1, 1, 0), (1, 1, 1), (2, 0, 0)\}$. At the two smallest values of q^2 and for the ensemble of gauge configurations considered, only the stochastic procedure provides time plateaux of enough good quality to allow the extraction of the pion form factor.

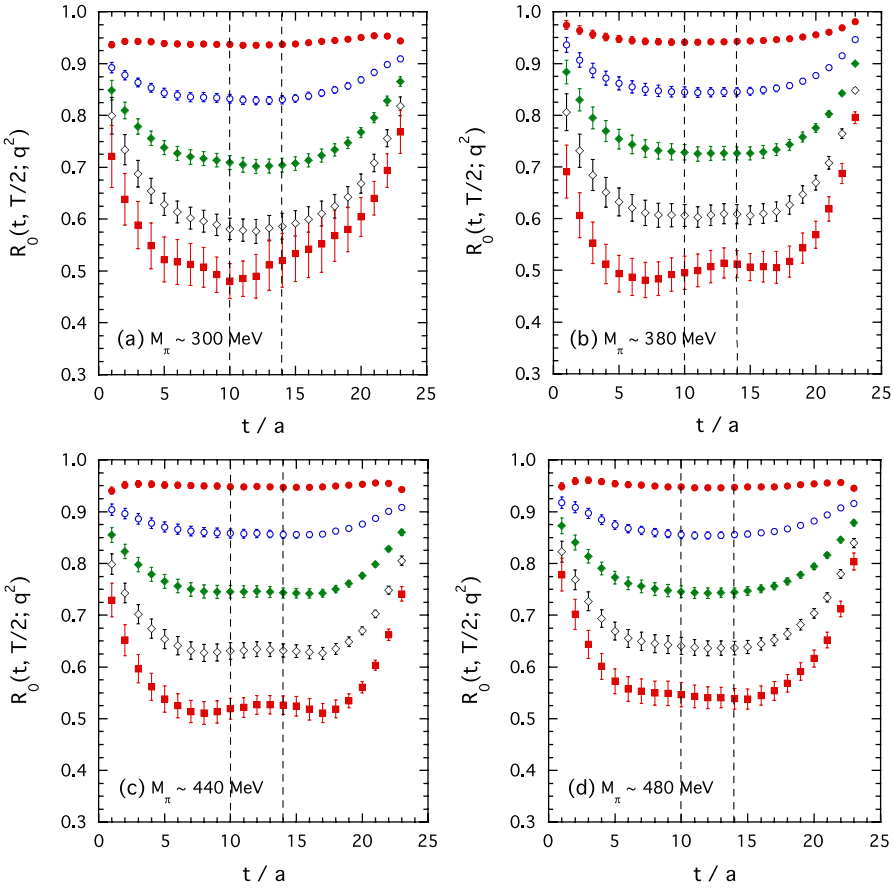

FIG. 6 (color online). Ratio $R_0(t, t'; q^2)$, defined by Eq. (25), at $t' = T/2$ versus the time distance t in lattice units, for $M_\pi \simeq 300$ MeV (a), $M_\pi \simeq 380$ MeV (b), $M_\pi \simeq 440$ MeV (c), $M_\pi \simeq 480$ MeV (d) at $\beta = 3.9$ and $V \cdot T = 24^3 \cdot 48a^4$. The full dots, open squares, full diamonds, open diamonds and full squares correspond to $a^2q^2 = -0.01, -0.03, -0.06, -0.10$ and -0.16, respectively. The dashed vertical lines identify the region $10 \leq t/a \leq 14$, where both the initial and the final pion ground states are isolated, so that the pion form factor $F_\pi(q^2)$ can be extracted.

gauge configurations for the stochastic and nonstochastic procedures in order to get the same total computational time.[7]

Despite the more limited ensemble of gauge configurations the stochastic approach provides a much better precision at the two lowest values of q^2 (a factor between ~ 2 and ~ 3). It also allows a very good determination of the form factor at the two highest values of q^2 considered in this study, where the procedure based on point-to-all propagators fails to give reliable signals even in the presence of a larger ensemble of gauge configurations.

As discussed in the previous section, the pion form factor $F_\pi(q^2)$ can be determined from the plateau of the ratio $R_0(t, t'; q^2)$, defined by Eq. (25), at large time distances. The quality of the time plateaux is illustrated in Fig. 6, while the momentum dependence of the extracted pion form factor $F_\pi(q^2)$ is shown in Fig. 7 for various values of M_π at $\beta = 3.9$ and $V \cdot T = 24^3 \cdot 48a^4$. We have checked that different choices of the time interval for the plateau region lead to values of $F_\pi(q^2)$, which are largely consistent within the statistical precision. The values of the pion form factor obtained for all the simulations of Table I are reported in the Appendix.

In the whole range of values of both q^2 and the quark mass, considered in this work, our lattice data can be fitted very nicely using a simple pole ansatz

$$F_\pi^{(\mathrm{pole})}(q^2) = \frac{1}{1 - q^2/M_{\mathrm{pole}}^2}, \tag{48}$$

as it is shown in Fig. 7. For comparison we also show the predictions of the vector meson dominance model, in which the parameter M_{pole} is fixed at the value of the lightest vector-meson mass (M_{VMD}) taken from Ref. [43]. The values obtained for M_{pole} by fitting our lattice points at $\beta = 3.9$ are given in Table II.

From Fig. 7 it can be seen that the VMD prediction, which considers the contribution of the lowest vector reso-

[7]Let us recall that the one-end-trick requires less computational time for a single inversion of the Dirac operator (a factor of about 1/3), but for each quark momentum a new inversion is needed by the use of twisted BCs.

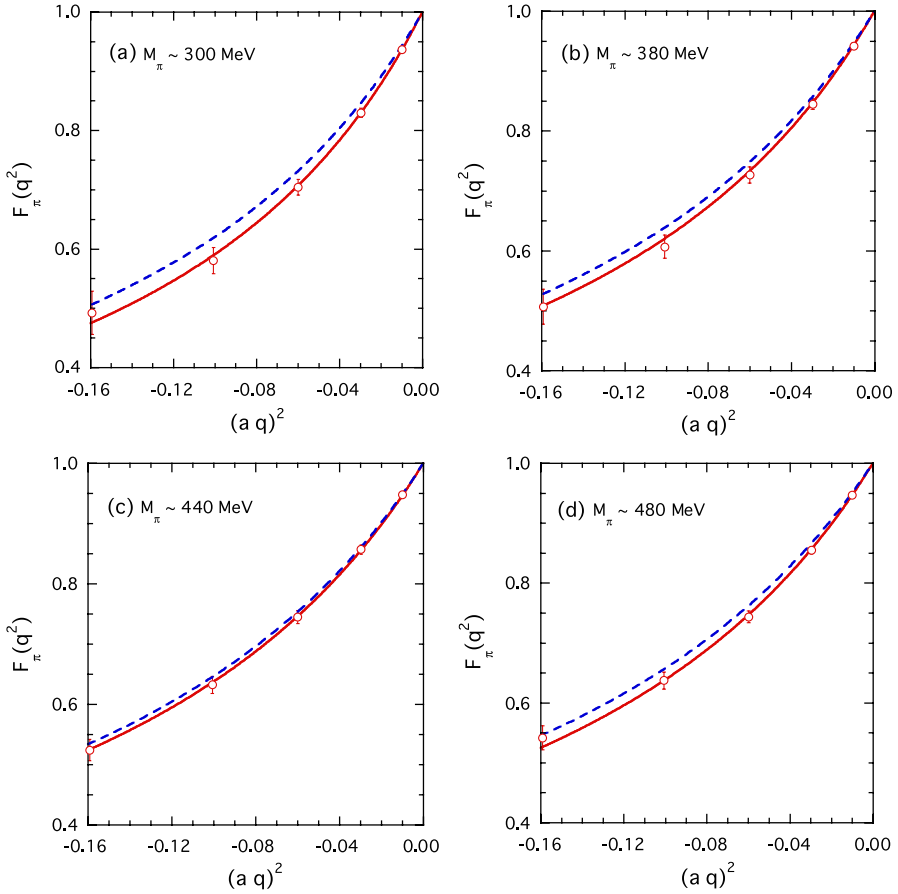

FIG. 7 (color online). Pion form factor $F_\pi(q^2)$, extracted from the plateau region $10 \leq t/a \leq 14$ of the ratio $R_0(t, T/2; q^2)$ (see Fig. 6), versus the squared 4-momentum transfer q^2 in lattice units, for $M_\pi \simeq 300$ MeV (a), $M_\pi \simeq 380$ MeV (b), $M_\pi \simeq 440$ MeV (c), $M_\pi \simeq 480$ MeV (d) at $\beta = 3.9$ and $V \cdot T = 24^3 \cdot 48a^4$. The solid line is the pole behavior (48) with the parameter $M_{\rm pole}$ fitted to the lattice points, while the dashed line is the VMD prediction with $M_{\rm pole}$ fixed at the value of the lightest vector-meson mass taken from Ref. [43].

nance only, is not exactly fulfilled, since $M_{\rm pole}$ turns out to be systematically lower than $M_{\rm VMD}$. However such a comparison might be plagued by systematic uncertainties affecting the lattice determination of the lightest vector-meson mass particularly at the lowest values of the pion mass (see Ref. [43]). Nevertheless, a simple extrapolation of $M_{\rm pole}$ to the physical point, based on a polynomial fit in terms of quark masses (see later Sec. V C), yields the value $M_{\rm pole}^{\rm phys} = 0.713 \pm 0.044$ GeV, which is lower than the VMD prediction $M_{\rm VMD}^{\rm phys} = M_\rho = 0.776$ GeV from PDG [22].

TABLE II. Values of the fit parameter $M_{\rm ploe}$ appearing in Eq. (48) obtained at $\beta = 3.9$ in lattice units.

Run	M_π (MeV)	$V \cdot T/a^4$	$aM_{\rm pole}$
R_1	$\simeq 260$	$32^3 \cdot 64$	0.359 ± 0.016
R_{2a}	$\simeq 300$	$32^3 \cdot 64$	0.363 ± 0.011
R_{2b}	$\simeq 300$	$24^3 \cdot 48$	0.379 ± 0.010
R_3	$\simeq 380$	$24^3 \cdot 48$	0.399 ± 0.014
R_4	$\simeq 440$	$24^3 \cdot 48$	0.420 ± 0.012
R_{5a}	$\simeq 480$	$24^3 \cdot 48$	0.419 ± 0.011
R_6	$\simeq 580$	$24^3 \cdot 48$	0.440 ± 0.005

Note also that, defining the squared *pole* radius in terms of Eq. (48) as

$$r^2_{\rm pole} \equiv 6/M^2_{\rm pole} = 6\left[\frac{dF_\pi^{\rm pole}(q^2)}{dq^2}\right]_{q^2=0}, \qquad (49)$$

the VMD model leads at the physical point to $r^2_{\rm pole} = 6/M^2_\rho \simeq 0.388$ fm^2, which underestimates by $\simeq 15\%$ the (quite precise) experimental value of the squared pion charge radius, $\langle r^2 \rangle^{\rm exp} = 0.452 \pm 0.011$ fm^2 [22]. On the contrary the value $M_{\rm pole}^{\rm phys} = 0.713 \pm 0.044$ GeV implies $r^2_{\rm pole} = 0.459 \pm 0.057$ fm^2 in nice agreement with the experimental charge radius.

D. Finite size effects

We have investigated the effects of the finite spatial extension L of our lattice boxes by comparing the results

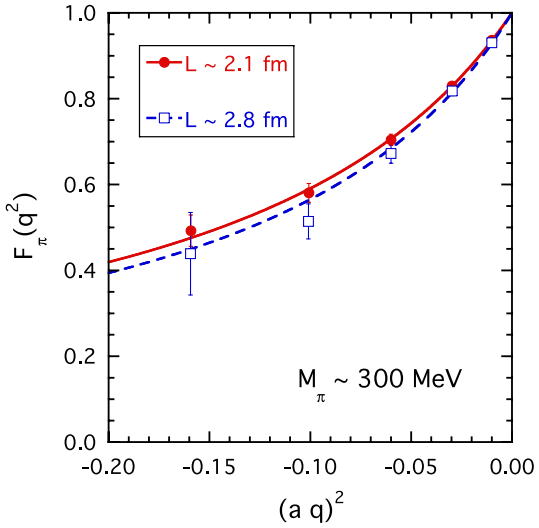

FIG. 8 (color online). Pion form factor $F_\pi(q^2)$ obtained for the runs R_{2a} (open squares) and R_{2b} (full dots), which correspond to different lattice boxes of size $L \simeq 2.8$ fm and $L \simeq 2.1$ fm, respectively. The solid and dashed lines are the results of the pole fit (48).

of runs R_{2a} and R_{2b}. In our simulations the latter has the smallest value of the quantity $M_\pi L$, which governs finite size effects (FSE) in the p-regime. The physical extension of the two boxes is $L \simeq 2.8$ fm and $L \simeq 2.1$ fm, respectively. The values of the angle θ are chosen differently at the two volumes in order to keep the values of q^2 fixed.

The results for the pion form factor are shown in Fig. 8, while a direct comparison of the results for the pion mass and decay constant as well as for the squared pole radius, $r^2_{\rm pole}$, is illustrated in Table III.

It can clearly be seen that FSE effects are larger on the pion form factor (or, equivalently, on the pole radius) with respect to the case of the pion mass and decay constant. They indeed amount to $\simeq 8\%$ on $r^2_{\rm pole}$ in contrast to a $\approx 2\%$ effect in the case of M_π and f_π. However we notice that FSE effects on $r^2_{\rm pole}$ are comparable to our statistical precision ($\simeq 6\%$), while they are much larger in the case of M_π and f_π ($0.2 \div 0.6\%$). Thus it is mandatory to include volume corrections to our results at least on the pion mass and decay constant.

On the theoretical side FSE on M_π and f_π have been studied with ChPT at NLO in Ref. [44] and using a resummed asymptotic formula in Ref. [45], where both leading and subleading exponential terms are taken into account and the chiral expansion is applied to the $\pi - \pi$ forward scattering amplitude. When the leading chiral representation of the latter is considered, the resummed approach coincides with the NLO result of Ref. [44]. Vice versa at NNLO the resummation technique includes only a part of the two-loop effects as well as of higher-loop effects. Recently the resummed approach has been positively checked against a full NNLO calculation of the pion mass in Ref. [46], showing that the missing two-loop contributions are actually negligible.

TABLE III. Values of the pion mass and decay constant from the high-statistics work of Ref. [24] and of the squared pole radius [see Eq. (49)] in lattice units for the runs R_{2a} and R_{2b}.

Run	L (fm)	aM_π	af_π	$r^2_{\rm pole}/a^2$
R_{2a}	$\simeq 2.8$	0.13377 (24)	0.06625 (16)	45.5 ± 2.8
R_{2b}	$\simeq 2.1$	0.13623 (65)	0.06459 (37)	41.7 ± 2.3

The volume corrections predicted by the resummed approach have been already considered in the analysis of the ETMC results for M_π and f_π carried out in Refs. [23–25].

On the contrary, until now, the theoretical investigation of FSE on the pion form factor is limited to the application of ChPT at NLO only. The case of periodic BCs is considered in Ref. [47], while twisted BCs are studied in Refs. [42,48] adopting two different reference frames, namely, the rest frame of the final meson [42] and the Breit one [48].

The sign of the volume effects on the pion form factor depends crucially on the absolute value and the spatial direction of the twisting vector $\vec{\theta}$. The sign of FSE on the charge radius turns out to be opposite between the cases of periodic (Ref. [47]) and twisted (Refs. [42,48]) BCs. When periodic BCs are used the extraction of the charge radius requires the use of the smallest available momentum, which is equal to $2\pi/L$. Such a restriction is absent with twisted BCs, and therefore volume effects are different.

Moreover the volume corrections depend on the reference frame: in the rest frame, besides the usual term related to the difference between the infinite volume loop integral and the sum over quantized momenta, there are two further contributions [42] arising from isospin and hypercubic invariance breakings generated by flavor-dependent twisted BCs. These two terms are vanishing in the Breit frame as shown in Ref. [48].

Only the results of Ref. [48], in which both the twisted BCs and the Breit reference frame are considered, can be directly applied to our data. Thus one gets

$$F_\pi(q^2;L) - F_\pi(q^2;\infty) = \frac{1}{f_\pi^2}\left\{\int_0^1 dx I_{1/2}\left[(1-2x)\frac{2\pi\vec{\theta}}{L}; M_\pi^2 - x(1-x)q^2\right] - I_{1/2}\left(\frac{2\pi\vec{\theta}}{L}; M_\pi^2\right)\right\} \quad (50)$$

with $q^2 = -4(2\pi\vec{\theta}/L)^2$ and

$$I_{1/2}\left(\frac{2\pi\vec{\theta}}{L}; M_\pi^2\right) = \frac{1}{2\pi^{3/2}L^2}\int_0^\infty d\tau \frac{1}{\sqrt{\tau}} e^{-\tau((M_\pi L/2\pi)^2)} \times \left[\prod_{i=1}^3 \Theta(\tau,\theta_i) - \left(\frac{\pi}{\tau}\right)^{3/2}\right] \quad (51)$$

where $\Theta(\tau, \theta)$ is defined after Eq. (47). The NLO volume corrections on the pion form factor expected for our run R_{2b} do not exceed half of the statistical error, and they are even smaller in the case of the run R_{2a} at the largest volume. The FSEs predicted by Eqs. (50) and (51) are quite small and have the same sign for all the choices of the twisting angle $\vec{\theta}$ made in this work. The NLO corrections go to the right direction decreasing slightly the differences between the pion form factor obtained at the two box sizes.

As for the squared pole radius, the shift with the lattice volume reported in Table III has the same sign expected from the volume correction (50). However the FSE calculated at NLO for the run R_{2b} corresponds to an increase of $\simeq 3\%$ only, that is almost a factor of 3 less than the observed FSE ($\simeq 8\%$). This suggests that higher-order chiral effects might be relevant on the pion form factor still for $M_\pi L \simeq 3$, although our statistical precision ($\simeq 6\%$) does not exclude FSEs on $r^2_{\rm pole}$ as small as the ones predicted at NLO by Eq. (50).

In the case of our runs R_1 and R_{2a}, which correspond to $M_\pi L \simeq 4$, the NLO volume corrections on $r^2_{\rm pole}$ are expected to be $\simeq 1\%$. After multiplying such a value by a factor ≈ 3 in order to take into account conservatively higher-loop effects, the expected FSE remains well below the statistical precision.

Therefore in this work we decide to analyze our form factor data using only simulations with $M_\pi L \gtrsim 4$, which means in practice that the run R_{2b} is excluded from our analyses of the pion form factor. On the contrary in case of the pion mass and decay constant we keep the run R_{2b} in the set of fitted data, but the FSEs, calculated through the resummed asymptotic formula of Ref. [45] at the NNLO accuracy for the $\pi - \pi$ forward scattering amplitude, will be taken into account (see Secs. V and VI).

E. Discretization effects

We have investigated the impact of lattice artifacts on the pion form factor by considering the runs R_{2c} and R_{5b} at the finer spacing $a \simeq 0.07$ fm (see Table I). These runs correspond to pion masses equal to $M_\pi \simeq 300$ MeV and $M_\pi \simeq 480$ MeV, respectively, which are very similar to those of the runs R_{2b} and R_{5a} at $a \simeq 0.09$ fm, while the physical lattice size is almost kept fixed ($L \simeq 2.1$ fm). Our results are shown in Fig. 9 in terms of the Sommer parameter r_0 instead of the lattice spacing a. The ratio r_0/a has been determined in the chiral limit at the two lattice spacings in Ref. [25], obtaining $r_0/a = 5.22 \pm 0.02$ at $\beta = 3.9$ and $r_0/a = 6.61 \pm 0.03$ at $\beta = 4.05$.

It can clearly be seen that the size of discretization effects is comparable to the statistical error at both pion masses. At the lowest pion mass there is a slight mismatch between the values of $M_\pi r_0$ corresponding to the runs R_{2b} and R_{2c}. Using the ChPT formulae at NNLO evaluated in Ref. [11], which will be used in the next sections, and adopting for the relevant LECs the values given in Ref. [33], we have estimated the correction due to the pion mass difference and applied it to the results of the run R_{2c} (see dotted line in Fig. 9). The correction is small, but reduces the impact of discretization effects, which now in terms of $r^2_{\rm pole}$ do not exceed $\simeq 5\%$ at both pion masses.

A more complete investigation of the scaling properties of the pion form factor, which requires the study of its mass dependence at two additional values of the lattice spacing, is needed and it is in progress.

In the next sections continuum ChPT will be applied to the chiral extrapolation of the results of the runs R_1, R_{2a}, R_3, R_4, R_{5a} and R_6, which correspond to a single lattice spacing ($a \simeq 0.09$ fm) and to a pion mass range between $\simeq 260$ MeV and $\simeq 580$ MeV with $M_\pi L \gtrsim 4$. The impact of lattice artifacts will be estimated by substituting the

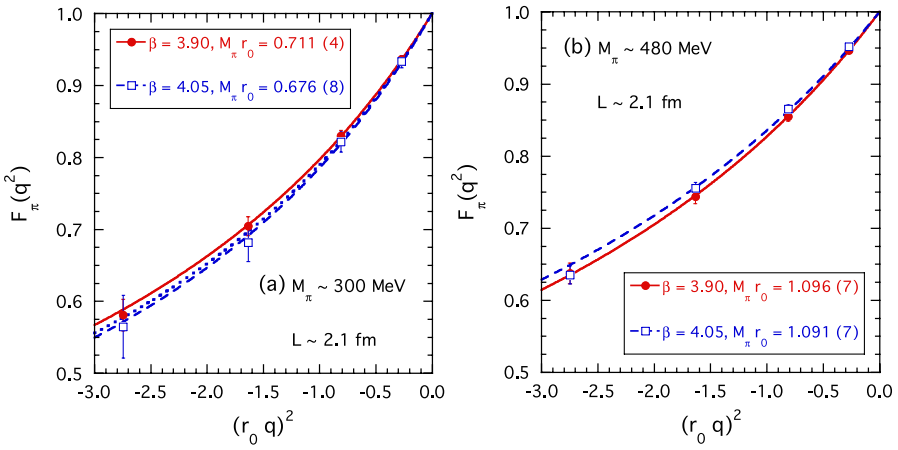

FIG. 9 (color online). Results of the pion form factor $F_\pi(q^2)$ versus q^2 in units of the Sommer parameter r_0, obtained for the runs R_{2b} (full dots) and R_{2c} (open squares) at $M_\pi \simeq 300$ MeV in (a), and for the runs R_{5a} (full dots) and R_{5b} (open squares) at $M_\pi \simeq 480$ MeV in (b). The physical lattice size is the same in both runs ($L \simeq 2.1$ fm). The solid and dashed lines are the results of the pole fit (48), while the dotted line in (a) corrects the dashed one for the pion mass difference (see text).

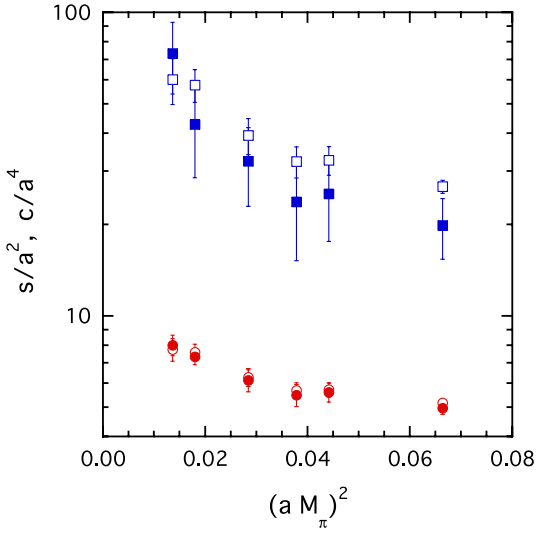

FIG. 10 (color online). The slope s (dots) and the curvature c (squares) of the pion form factor [see Eq. (52)] versus the squared pion mass in lattice units, for the runs R_1, R_{2a}, R_3, R_4, R_{5a} and R_6. Open dots and squares correspond to the results of the pole fit given by Eqs. (53) and (54), respectively. Full markers are the results obtained with the cubic fit (55).

results of the runs R_{2a} and R_{5a} with those of the runs R_{2c} and R_{5b}, respectively.

V. SLOPE AND CURVATURE OF THE PION FORM FACTOR

The slope s and the curvature c of the pion form factor are defined from the expansion in q^2

$$F_\pi(q^2) = 1 + sq^2 + cq^4 + \mathcal{O}(q^6). \tag{52}$$

In terms of the pole ansatz (48) the slope is given by

$$s_{\rm pole} = \frac{1}{M^2_{\rm pole}} = \frac{r^2_{\rm pole}}{6}, \tag{53}$$

while the curvature is constrained to be

$$c_{\rm pole} = s^2_{\rm pole} = \frac{1}{M^4_{\rm pole}} = \left(\frac{r^2_{\rm pole}}{6}\right)^2. \tag{54}$$

We have therefore compared the slope and curvature obtained from the pole ansatz (48) with those of a simple cubic fit in q^2

$$F^{\rm (cub)}_\pi(q^2) = 1 + s_{\rm cub}q^2 + c_{\rm cub}q^4 + d_{\rm cub}q^6. \tag{55}$$

The results obtained by including in the fitting procedure the form factor corresponding to the four highest, negative values of q^2 are shown in Fig. 10 (see also Table IV).[8] It can be seen that the two determinations of the slope are in very good agreement, and the results for the curvature are consistent within the statistical errors, which turn out to be lower in the case of the pole fit.

In what follows we take as our best estimates the values of the slope and the curvature coming from the pole ansatz. The former ones, expressed in physical units using the value $a = 0.087$ fm from Ref. [23], are collected in the third column of Table IV and shown in Fig. 11, where they are compared with the available results of other lattice collaborations that employ $O(a)$-improved lattice actions and unquenched gauge configurations. It can be seen that all the determinations of the pion charge radius exhibit a quite similar mass dependence, indicating that lattice artifacts are presumably under control. The results labeled as "QCDSF/UKQCD" in Fig. 11 do not correspond to the original ones reported in Ref. [19]. There the lattice spacing, instead of the Sommer parameter r_0, was assumed to depend on the sea quark mass, and such a procedure reintroduces non-negligible lattice artifacts. The "QCDSF/UKQCD" results shown in Fig. 11 are obtained after properly extrapolating the ratio r_0/a to the chiral limit.[9]

TABLE IV. Values of the pion mass, charge radius and curvature, determined from the pole (53) and (54) and cubic (55) fits, for the various ETMC runs. Physical units are used taking for the lattice spacing the value $a = 0.087$ fm from Ref. [23]. The uncertainties are statistical (jackknife) errors.

Run	M_π (MeV)	$r^2_{\rm pole} \equiv 6s_{\rm pole}$ (fm^2)	$c_{\rm pole}$ (10^{-3} fm^4)	$r^2_{\rm cub} \equiv 6s_{\rm cub}$ (fm^2)	$c_{\rm cub}$ (10^{-3} fm^4)
R_1	265	0.352 ± 0.030	3.44 ± 0.59	0.364 ± 0.028	4.20 ± 1.12
R_{2a}	304	0.345 ± 0.021	3.30 ± 0.40	0.333 ± 0.020	2.45 ± 0.82
R_3	383	0.285 ± 0.019	2.25 ± 0.31	0.278 ± 0.023	1.85 ± 0.54
R_4	441	0.258 ± 0.015	1.85 ± 0.22	0.249 ± 0.021	1.36 ± 0.49
R_{5a}	477	0.259 ± 0.014	1.87 ± 0.20	0.254 ± 0.018	1.45 ± 0.44
R_6	584	0.234 ± 0.006	1.53 ± 0.07	0.225 ± 0.010	1.14 ± 0.26

[8]The lattice points at the lowest, negative value of q^2 are the noisiest data (see Fig. 7 and also Fig. 6 for the corresponding time plateaux). The inclusion of these data in the fitting procedure does not change significantly the determination of the various parameters appearing in Eqs. (53) and (55).

[9]We thank J. Zanotti for providing us with the extrapolated values of r_0/a at the chiral point.

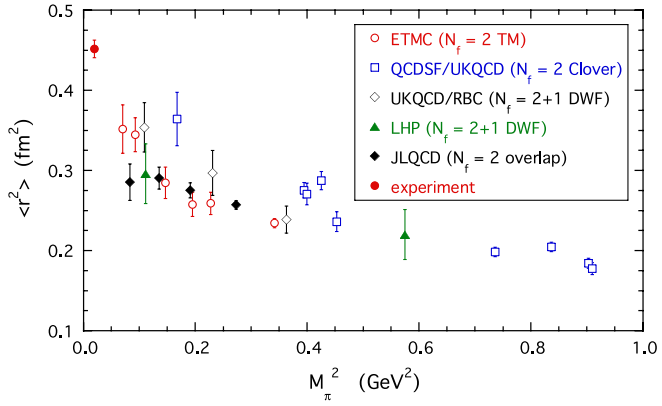

FIG. 11 (color online). The squared pion charge radius versus the squared pion mass. Open dots: this work (see third column of Table IV). Open squares: results from Ref. [19] corrected as explained in the text. Open diamonds, full triangles, full diamonds correspond to Refs. [14,20,21], respectively. The full dot represents the experimental value of the squared pion charge radius $\langle r^2\rangle^{\rm exp} = 0.452 \pm 0.011$ fm^2 from PDG [22].

A. ChPT formulae at NNLO

In Ref. [11] the pion form factor, as well as the pion mass and decay constant, have been calculated in continuum SU(2) ChPT at NNLO in infinite volume using a modified minimal subtraction ($\overline{\rm MS}$) scheme to regulate the infinities. Using the quark mass $\hat{m}$ as the expansion parameter, one has

$$M_\pi^2 = 2B\hat{m} + [M_\pi^2]_{\rm NLO} + [M_\pi^2]_{\rm NNLO} + \mathcal{O}(\hat{m}^4), \quad (56)$$

$$[M_\pi^2]_{\rm NLO} = 2B\hat{m}\cdot 2x_2\left[2\ell_3^r + \frac{1}{2}L(\mu)\right], \quad (57)$$

$$[M_\pi^2]_{\rm NNLO} = 2B\hat{m}\cdot 4x_2^2\left\{\frac{1}{N}\left[\ell_1^r + 2\ell_2^r - \frac{13}{3}L(\mu)\right] + \frac{163}{96}\frac{1}{N^2} - \frac{7}{2}k_1 - 2k_2 + 4\ell_3^r(\ell_4^r - \ell_3^r) - \frac{9}{4}k_3 + \frac{1}{4}k_4 + r_M^r + \Delta_M\left(\Delta_M - \Delta_F + \frac{1}{2N}\right)\right\}, \quad (58)$$

$$f_\pi = F + [f_\pi]_{\rm NLO} + [f_\pi]_{\rm NNLO} + \mathcal{O}(\hat{m}^3), \quad (59)$$

$$[f_\pi]_{\rm NLO} = 2Fx_2[\ell_4^r - L(\mu)], \quad (60)$$

$$[f_\pi]_{\rm NNLO} = 4Fx_2^2\left\{\frac{1}{N}\left[-\frac{1}{2}\ell_1^r - \ell_2^r + \frac{29}{12}L(\mu)\right] - \frac{13}{192}\frac{1}{N^2} + \frac{7}{4}k_1 + k_2 + 2\ell_4^r(\ell_4^r - \ell_3^r) - \frac{5}{4}k_4 + r_F^r + \frac{1}{2}\Delta_F(\Delta_M - \Delta_F) - \frac{1}{N}\Delta_M\right\}, \quad (61)$$

$$\langle r^2\rangle = [\langle r^2\rangle]_{\rm NLO} + [\langle r^2\rangle]_{\rm NNLO} + \mathcal{O}(\hat{m}^2), \quad (62)$$

$$[\langle r^2\rangle]_{\rm NLO} = -\frac{2}{F^2}\left(6\ell_6^r + L(\mu) + \frac{1}{N}\right), \quad (63)$$

$$[\langle r^2\rangle]_{\rm NNLO} = 4\frac{x_2}{F^2}\left\{\frac{1}{N}\left[-2\ell_4^r + \frac{31}{6}L(\mu) + \frac{13}{192} - \frac{181}{48N}\right] - 3k_1 + \frac{3}{2}k_2 - \frac{1}{2}k_4 + 3k_6 - 12\ell_4^r\ell_6^r + 6r_1^r + \Delta_F\left(6\ell_6^r + L(\mu) + \frac{1}{N}\right) - \frac{1}{N}\Delta_M\right\}, \quad (64)$$

$$c = [c]_{\rm NLO} + [c]_{\rm NNLO} + \mathcal{O}(\hat{m}), \quad (65)$$

$$[c]_{\rm NLO} = \frac{2}{60NF^4x_2}, \quad (66)$$

$$[c]_{\rm NNLO} = \frac{4}{F^4}\left\{\frac{1}{N}\left[-\frac{13}{540}L(\mu) + \frac{1}{720} - \frac{8429}{25920N}\right] + \frac{1}{12}k_1 - \frac{1}{24}k_2 + \frac{1}{24}k_6 + \frac{1}{3N}\left(\ell_1^r - \frac{1}{2}\ell_2^r + \frac{1}{10}\ell_4^r + \frac{1}{2}\ell_6^r\right) + r_2^r - \frac{1}{60N}(\Delta_M + \Delta_F)\right\}, \quad (67)$$

where $2B\hat{m}$ is the celebrated GMOR term, F is the pion decay constant in the chiral limit (f_π is normalized such that $f_\pi \approx 130$ MeV at the physical point) and

$$N \equiv (4\pi)^2, \qquad x_2 \equiv \frac{2B\hat{m}}{F^2}, \qquad L(\mu) \equiv \frac{1}{N}\log\left(\frac{2B\hat{m}}{\mu^2}\right),$$
$$k_i \equiv [4\ell_i^r - \gamma_i L(\mu)]L(\mu), \qquad \Delta_M \equiv 2\ell_3^r + \frac{1}{2}L(\mu),$$
$$\Delta_F \equiv 2[\ell_4^r - L(\mu)]. \quad (68)$$

The constants ℓ_i^r are the finite part of the coupling constants appearing in the $O(p^4)$ Lagrangian after the application of the $\overline{\rm MS}$ procedure, and their values depend on the renormalization scale μ through the anomalous dimensions γ_i as $\mu^2 d\ell_i^r/d\mu^2 = -\gamma_i/2N$. The coefficients γ_i are calculated in Ref. [10], and those relevant in this work are given by: $\gamma_1 = 1/3$, $\gamma_2 = 2/3$, $\gamma_3 = -1/2$, $\gamma_4 = 2$, $\gamma_6 = -1/3$. The four constants r_M^r, r_F^r, r_1^r, r_2^r denote the contributions of the $O(p^6)$ Lagrangian after $\overline{\rm MS}$ subtraction. Though the values of all the above constants depend on μ, at each order in the chiral expansion the physical observables are independent (as they should be) of the value of the renormalization scale μ.

At LO only two chiral parameters appear, namely B (related to the chiral condensate) and F. At NLO three further LECs, ℓ_3^r, ℓ_4^r and ℓ_6^r, are present. At NNLO the total number of LECs increases up to 11 due to the inclusion of ℓ_1^r, ℓ_2^r, r_M^r, r_F^r, r_1^r and r_2^r.

We notice that the NNLO terms for the charge radius (64) and the curvature (67) do not depend upon the LECs ℓ_1^r and ℓ_2^r separately, but only through the linear combination $(\ell_1^r - \ell_2^r/2)$. However different linear combinations of ℓ_1^r and ℓ_2^r appear in the NNLO terms of both the pion mass (58) and decay constant (61). Therefore the LECs ℓ_1^r and ℓ_2^r can be determined by a simultaneous analysis of the charge radius (and/or the curvature) together with the pion mass and decay constant.

In what follows the $O(p^4)$ constants ℓ_i^r will be substituted by scale-invariant quantities, $\bar{\ell}_i$, defined via the relations

$$\ell_i^r \equiv \frac{\gamma_i}{2N}[\bar{\ell}_i + NL(\mu)]. \tag{69}$$

The new quantities, which depend (logarithmically) on the quark mass, can be expressed as $\bar{\ell}_i = \log(\Lambda_i^2/2B\hat{m})$, and their values are commonly given at the physical point.

We notice that in Ref. [11] the quark mass is not actually used as the expansion parameter. Instead of it the physical pion mass and decay constant are adopted. In order to recover the formulae of Ref. [11] it is enough to replace in Eqs. (56)–(68) x_2 with M_π^2/f_π^2, $L(\mu)$ with $(1/N)\cdot\log(M_\pi^2/\mu^2)$ and to set $\Delta_M = \Delta_F = 0$ wherever they appear explicitly.

As explained in Sec. IV D we apply to the pion mass and decay constant the corrections for FSE computed in Ref. [45]. Using again the quark mass $\hat{m}$ as the expansion parameter, one gets

$$\frac{M_\pi(L) - M_\pi}{M_\pi} = \frac{2x_2}{N}\sum_{n=1}^{\infty}\frac{m(n)}{\lambda_n}\Bigg\{K_1(\lambda_n) - \frac{2x_2}{N}\Bigg[K_1(\lambda_n)\left(-\frac{55}{18} + 4\bar{\ell}_1 + \frac{8}{3}\bar{\ell}_2 - \frac{5}{2}\bar{\ell}_3 - 2\bar{\ell}_4\right) + \frac{K_2(\lambda_n)}{\lambda_n}\left(\frac{112}{9} - \frac{8}{3}\bar{\ell}_1 - \frac{32}{3}\bar{\ell}_2\right)$$
$$+ \frac{13}{3}g_0K_1(\lambda_n) - \frac{1}{3}(40g_0 + 32g_1 + 26g_2)\frac{K_2(\lambda_n)}{\lambda_n} + \frac{N}{2}[\Delta_M\lambda_nK_0(\lambda_n) + 2\Delta_FK_1(\lambda_n)]\Bigg]\Bigg\} + \mathcal{O}(\hat{m}^3), \tag{70}$$

$$\frac{f_\pi(L) - f_\pi}{f_\pi} = -2\frac{2x_2}{N}\sum_{n=1}^{\infty}\frac{m(n)}{\lambda_n}\Bigg\{2K_1(\lambda_n) - \frac{2x_2}{N}\Bigg[K_1(\lambda_n)\left(-\frac{7}{9} + 2\bar{\ell}_1 + \frac{4}{3}\bar{\ell}_2 - 3\bar{\ell}_4\right) + \frac{K_2(\lambda_n)}{\lambda_n}\left(\frac{112}{9} - \frac{8}{3}\bar{\ell}_1 - \frac{32}{3}\bar{\ell}_2\right)$$
$$+ \frac{1}{6}(8g_0 - 13g_1)K_1(\lambda_n) - \frac{1}{3}(40g_0 - 12g_1 - 8g_2 - 13g_3)\frac{K_2(\lambda_n)}{\lambda_n} + N[\Delta_M\lambda_nK_0(\lambda_n) + 2\Delta_FK_1(\lambda_n)]\Bigg]\Bigg\}$$
$$+ \mathcal{O}(\hat{m}^3), \tag{71}$$

where $K_{0,1,2}$ are modified Bessel functions, the values of the multiplicities $m(n)$ are given in Ref. [45] and

$$\lambda_n \equiv \sqrt{n}\sqrt{2B\hat{m}}L, \qquad g_0 \equiv 2 - \frac{\pi}{2}, \qquad g_1 \equiv \frac{\pi}{4} - \frac{1}{2},$$
$$g_2 \equiv \frac{1}{2} - \frac{\pi}{8}, \qquad g_3 \equiv \frac{3\pi}{16} - \frac{1}{2}. \tag{72}$$

Notice that in Eqs. (70) and (71) no further LEC is introduced with respect to Eqs. (56)–(61).

In order to recover the formulae of Ref. [45], where the physical pion mass and decay constant are adopted as expansion parameters, it is enough to replace in Eqs. (70) and (71) x_2 with M_π^2/f_π^2, λ_n with $\sqrt{n}M_\pi L$ and to set $\Delta_M = \Delta_F = 0$.

B. Chiral fits

Let us now apply Eqs. (56)–(67) to the analyses of the quark mass dependence of our results. As explained in the previous section the set of lattice data chosen for the fitting procedure is given by the results of the runs R_1, R_{2a}, R_3, R_4, R_{5a} and R_6 for four quantities: the pion mass and decay constant, the charge radius and the curvature of the pion form factor. In case of the pion mass and decay constant also the results of the run R_{2b} are considered and the FSE corrections given by Eqs. (70) and (71) are applied.

Since each run corresponds to an independent ensemble of gauge configurations a bootstrap procedure is applied in order to combine all the jackknives in different ways (1000 samples are used in practice). The statistical uncertainties, which are reported hereafter, are therefore bootstrap errors.

In order to fix the lattice spacing and the up/down quark mass the experimental values of the pion mass and decay constant ($M_\pi^{\rm phys} = 134.98$ MeV and $f_\pi^{\rm phys} = 130.7 \pm 0.4$ MeV from Ref. [22]) are used.[10] We determine first the value of the bare quark mass am_π, at which the pion assumes its physical mass, by requiring that the ratio M_π/f_π from Eqs. (56) and (59) takes the experimental value $134.98/130.7 \simeq 1.033$. Second, using the physical value $f_\pi^{\rm phys}$ the lattice spacing a is determined. The value of the renormalized light-quark mass in the $\overline{\rm MS}$ scheme, $m^{\overline{\rm MS}}(2\ {\rm GeV})$, is obtained from am_π by considering the determination of the nonperturbative (multiplicative) renormalization constant $Z_m = 1/Z_P$, evaluated using the RI-MOM scheme in Ref. [41], and the matching factor with the $\overline{\rm MS}$ scheme, which is known up to four loops [51].

[10] In order to account for the e.m. isospin breaking effects which are not introduced in the lattice simulations, we use the experimental value of the neutral pion mass in accord with Refs. [49,50].

TABLE V. Values of the chiral parameters, the lattice spacing and the renormalized quark mass $\hat{m} = m^{\overline{MS}}(2\ \mathrm{GeV})$ at the physical point for various ChPT analyses (see text). For consistency with $\hat{m}$, the parameter B is given in the $\overline{MS}$ scheme at a scale equal to 2 GeV. The values of the parameters r_M^r, r_F^r, r_1^r and r_2^r are given at the ρ-meson mass scale. In the case of the NLO analysis the parameters $\bar{\ell}_1$ and $\bar{\ell}_2$ are used only for evaluating FSEs, while the parameter $\bar{\ell}_6$ is fixed by the experimental value of the pion charge radius. The latter is not included in the NNLO analyses. The uncertainties are statistical (bootstrap) errors only.

Parameter	NLO	NNLO	NNLO + $\langle r^2 \rangle_S^{\mathrm{exp}}$
$2B$ (GeV)	5.21 ± 0.05	5.19 ± 0.42	4.89 ± 0.08
F (MeV)	121.7 ± 1.1	121 ± 10	122.5 ± 0.9
$\bar{\ell}_3$	3.48 ± 0.12	5.0 ± 4.0	3.1 ± 0.7
$\bar{\ell}_4$	4.67 ± 0.06	5.2 ± 1.8	4.39 ± 0.14
$\bar{\ell}_6$	14.59 ± 0.03	14.9 ± 2.2	15.9 ± 1.3
$\bar{\ell}_1$	−0.4 [33]	0.3 ± 3.4	−1.3 ± 1.4
$\bar{\ell}_2$	4.3 [33]	5.3 ± 1.1	5.1 ± 1.1
$r_M^r \cdot 10^4$	⋯	−0.1 ± 1.1	−0.60 ± 0.29
$r_F^r \cdot 10^4$	⋯	−0.5 ± 1.5	−0.15 ± 0.14
$r_1^r \cdot 10^4$	⋯	−0.95 ± 0.15	−0.92 ± 0.15
$r_2^r \cdot 10^4$	⋯	0.70 ± 0.17	0.77 ± 0.04
a (fm)	0.0861 ± 0.0007	0.0863 ± 0.0047	0.0884 ± 0.0006
$\hat{m}^{\mathrm{phys}}$ (MeV)	3.60 ± 0.08	3.6 ± 0.6	3.81 ± 0.08
χ^2/d.o.f.	0.72	0.91	0.88

We start with a ChPT analysis at NLO including our lattice data only for the pion mass and decay constant up to $M_\pi \simeq 500$ MeV in order to compare with the ETMC NLO analyses of Refs. [23,24,34]. The main differences are: i) the use of a single lattice spacing ($a \simeq 0.09$ fm) both in the present work and in Refs. [23,24], while the results obtained from two lattice spacings ($a \simeq 0.07$ and 0.09 fm) are taken into account in Ref. [34]; ii) a better statistical accuracy of the data for M_π and f_π in Refs. [23,24,34] due to the use of all the (correlated) trajectories produced by the ETM Collaboration with respect to the present work in which only a subset of 240 (uncorrelated) trajectories are employed; iii) the presence of the results of the run R_1 at $M_\pi \simeq 260$ MeV in the present work and in Ref. [34] at variance with Refs. [23,24].

Following Ref. [24] the FSE correction can be evaluated beyond NLO using Eqs. (70) and (71) and adopting for the unknown LECs $\bar{\ell}_1$ and $\bar{\ell}_2$ the central values given in Ref. [33]. The values obtained for the fitting parameters (the LECs of the chiral Lagrangian) are given in the second column of Table V, while the best fit at NLO, including the FSE corrections given by Eqs. (70) and (71), is shown in Fig. 12 by the dashed lines.

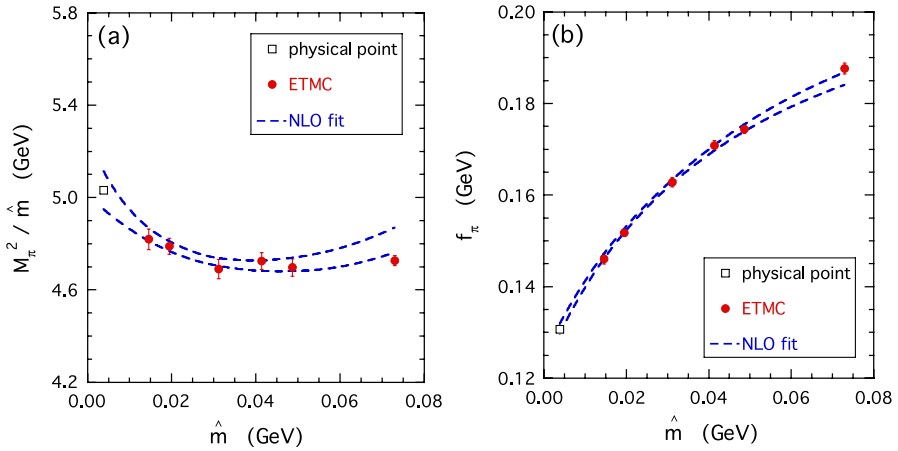

FIG. 12 (color online). The ratio of the squared pion mass to the renormalized quark mass $\hat{m} = m^{\overline{\mathrm{MS}}}(2\ \mathrm{GeV})$ (a) and the pion decay constant (b) versus $\hat{m}$ in physical units. The points at the highest value of $\hat{m}$ are not included in the analysis. The dots are the ETMC results, corrected by the FSE effects given by Eqs. (70) and (71), and the squares represent the experimental value for each quantity from Ref. [22]. The dashed lines correspond to the region selected at 1σ level by the ChPT analysis at NLO [see Eqs. (56), (57), (59), and (60)]. The values of the fitting parameters are listed in the second column of Table V.

TABLE VI. Values of the quantities $aM_\pi(L = 24a)/aM_\pi(L = 32a) - 1$ and $af_\pi(L = 24a)/af_\pi(L = 32a) - 1$ from the runs R_{2a} and R_{2b} at a pion mass of $\simeq 300$ MeV. The lattice results correspond to the values given in Table III. The theoretical results are those corresponding to Eqs. (70) and (71) using for the relevant LECs the values reported in the second column of Table V.

	Lattice (%)	Theoretical (%)
$aM_\pi(L = 24a)/aM_\pi(L = 32a) - 1$	+1.8(5)	+1.2
$af_\pi(L = 24a)/af_\pi(L = 32a) - 1$	−2.5(6)	−2.5

It can be seen that the values of all the chiral parameters, in particular, of the LECs $\bar{\ell}_3$ and $\bar{\ell}_4$, as well as the values of the lattice spacing a and the light-quark mass $\hat{m}^{\rm phys}$, are consistent with the findings of Refs. [23,24,34]. Note also that the statistical precision of the extracted values of $\bar{\ell}_3$ and $\bar{\ell}_4$ is very similar in this work and in Refs. [23,24,34].

The theoretical evaluation of FSE effects given by Eqs. (70) and (71) appears to work quite well. Indeed after applying the FSE corrections, the pion masses and decay constants corresponding to the runs R_{2a} (at $L = 32a$) and R_{2b} (at $L = 24a$) become consistent within 1 standard deviation, as shown in Table VI.

We have checked that the full exclusion of the run R_{2b} from our analyses does not have any significant impact on the chiral fits as well as on the values obtained for the chiral parameters. Therefore, since the runs R_{2a} and R_{2b} are compatible once theoretical FSEs are included through Eqs. (70) and (71), in what follows we shall not show the results of the run R_{2b} in the figures (i.e., we show only lattice data having $M_\pi L \gtrsim 4$) and we will always apply to the pion mass and decay constant the FSE corrections given by Eqs. (70) and (71).

The quality of the NLO fit shown in Fig. 12 is quite remarkable, leaving apparently little room for higher-order corrections even at the highest pion mass ($\simeq 580$ MeV), though the latter point is not included in the fitting procedure. However we now show that the same does not hold for the charge radius and the curvature of the pion form factor.

The NLO prediction for the charge radius [see Eq. (63)] depends in practice only on one LEC, $\bar{\ell}_6$, being F fixed by the analysis of the pion decay constant with a precision of the level of $\simeq 1\%$ (see the second column of Table V). Note also that both the derivative of $[\langle r^2\rangle]_{\rm NLO}$ with respect to the quark mass and the curvature $[c]_{\rm NLO}$ (see Eq. (66)) are independent of $\bar{\ell}_6$ and therefore basically parameter-free.

The value of the LEC $\bar{\ell}_6$ can be determined from the experimental value of the squared charge radius, $\langle r^2\rangle^{\rm exp} = 0.452 \pm 0.011$ fm^2 [22], since the latter is expected to be dominated by the NLO term (63). This leads to $\bar{\ell}_6 = 14.59 \pm 0.03$ (see the second column of Table V). The corresponding NLO predictions for the charge radius and the curvature are shown in Fig. 13 by the dashed lines. They significantly overestimate our lattice data for the charge radius and largely underestimate those for the curvature.

Alternatively we have excluded the experimental value of the charge radius and included in the fitting procedure the lattice data of the charge radius for pion masses up to $\simeq 500$ MeV (i.e., for $\hat{m} \lesssim 0.05$ GeV) obtaining $\bar{\ell}_6 = 11.6 \pm 0.3$ (with χ^2/d.o.f. $\simeq 1.2$). The corresponding NLO predictions are shown in Fig. 13 by the dotted lines. At the physical point the charge radius is

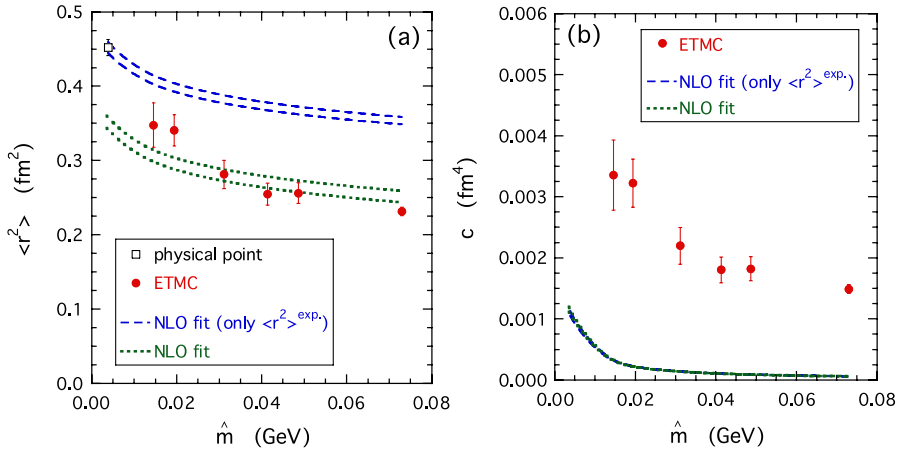

FIG. 13 (color online). The squared charge radius (a) and the curvature (b) of the pion form factor versus the renormalized quark mass $\hat{m}$ in physical units. The dots are our lattice results and the square represents the experimental value of the squared charge radius [22]. The dashed and dotted lines represent the region selected at 1σ level by the ChPT predictions at NLO given by Eqs. (63) and (66). In the case of the dashed lines the value of the LEC $\bar{\ell}_6$ is fixed by the experimental charge radius, while in the case of the dotted lines it is obtained by including in the fitting procedure our lattice data of the charge radius for pion masses up to $\simeq 500$ MeV (i.e., for $\hat{m} \lesssim 0.05$ GeV).

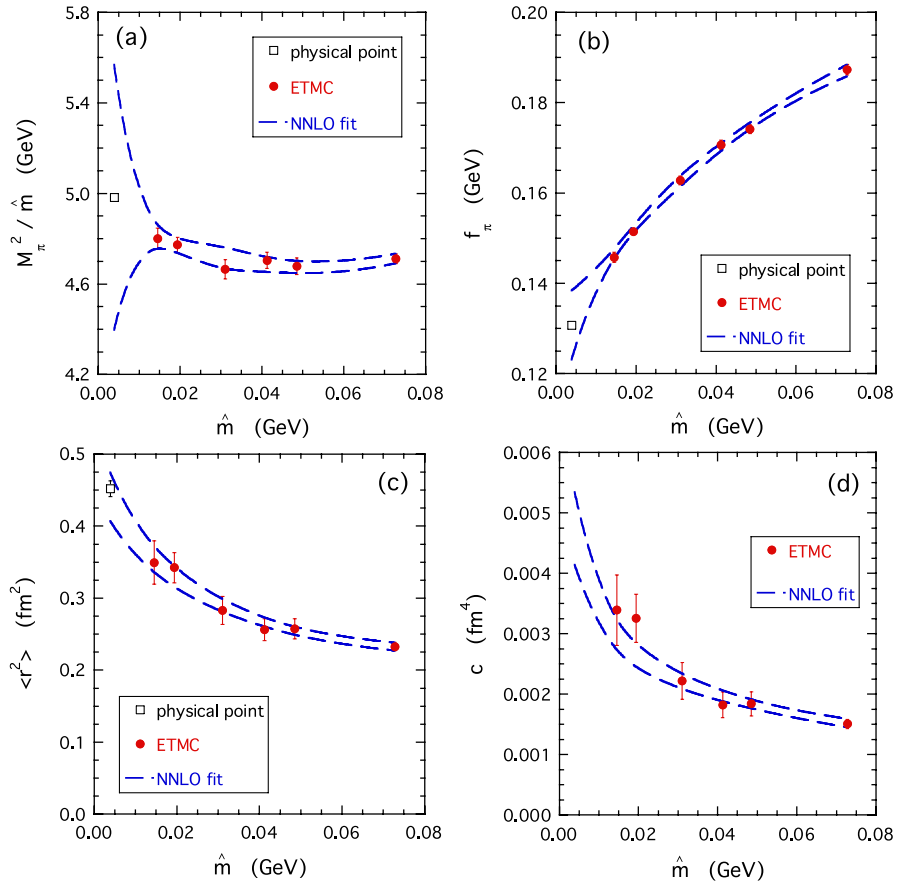

FIG. 14 (color online). The ratio $M_\pi^2/\hat{m}$ (a), the pion decay constant (b), the charge radius (c) and the curvature (d) of the pion form factor versus the renormalized quark mass $\hat{m}$ in physical units. The dots are our lattice results and the squares represent the corresponding experimental values from PDG [22]. The dashed lines correspond to the region selected at 1σ level by the ChPT fit at NNLO based on Eqs. (56)–(67). The values of the fitting parameters are listed in the third column of Table V. The experimental value of the pion charge radius is not included in the fitting procedure.

$\langle r^2 \rangle^{\rm phys} = 0.352 \pm 0.008$ fm^2 in clear contradiction with the experimental value.[11]

Moreover, since the curvature is independent on $\bar{\ell}_6$, any NLO fit is unable to provide enough large values of the curvature consistent with the relation (54), i.e., with the pole behavior of the pion form factor observed in Sec. IV C. Such a finding suggests that an NLO analysis of the pion form factor is applicable only to quite low values of $|q^2|$ (see later Sec. VI).

Thus, both the NLO results shown in Fig. 13 and the smallness of the systematic effects due to finite volumes and lattice spacings, estimated in Secs. IV D and IV E indicate that the quark mass dependences of our lattice data for both the charge radius and the curvature require taking into account chiral effects beyond the NLO.

The results of the fit performed using ChPT at NNLO [i.e. based on Eqs. (56)–(67)] are shown in Fig. 14, while the values of the fitting parameters are listed in the third column of Table V with the renormalization scale μ fixed at the physical ρ-meson mass. Notice that the experimental value of the pion charge radius is not included in the fitting procedure.

As already found in Ref. [24], the inclusion of NNLO effects leads to quite large uncertainties in the values of all the LECs, in particular, both for the LECs $\bar{\ell}_3$ and $\bar{\ell}_4$ appearing at NLO and NNLO, and for the LECs $\bar{\ell}_1$ and $\bar{\ell}_2$ appearing only at NNLO. Nevertheless the uncertainties in the chiral fits shown in Fig. 14 are of the order of the statistical errors in the mass range of the lattice points. This means that the large uncertainties reported in the third column of Table V are strongly correlated; the effect of the variation of one fitting parameter can be always compensated by those generated by the variations of the other

[11] If only the lattice data of the charge radius for the two lowest pion masses ($M_\pi \lesssim 300$ MeV) are considered, the value of $\bar{\ell}_6$ becomes 12.8 ± 0.5 (with $\chi^2/\text{d.o.f.} \simeq 0.65$) and the predicted charge radius at the physical point is $\langle r^2 \rangle^{\rm phys} = 0.393 \pm 0.017$ fm^2, which still deviates from the experimental value by 3 standard deviations.

parameters. However when we extrapolate the chiral predictions for the pion mass and decay constant outside the mass range of the lattice data towards the chiral point we end up with rather large uncertainties as shown in Fig. 14.

Such a situation is clearly unsatisfactory both for a precise extraction of the LECs and for the extrapolation to the physical point. The inclusion of the experimental values of the pion charge radius and curvature in the set of fitted data can obviously reduce the uncertainties in the extraction of the chiral parameters, but in this way the predictive power of the chiral fits is lost.

Thus we look for an observable which should be: i) unrelated to the vector form factor of the pion, ii) known experimentally and iii) whose chiral expansion at NLO contains one of the LECs, let us say $\bar{\ell}_3$ or $\bar{\ell}_4$. In this way the experimental value of such an observable, expected to be dominated by the NLO contribution, can constrain sufficiently the range of the variability of one of the LECs. In turn this could be beneficial to reduce the uncertainties of all our fitting parameters.

A possible, appropriate choice is the squared radius $\langle r^2\rangle_S$ of the pion "scalar" form factor, defined as

$$\langle r^2\rangle_S \equiv= \frac{6}{F_\pi^S(0)}\left[\frac{dF_\pi^S(q^2)}{dq^2}\right]_{q^2=0}, \tag{73}$$

where

$$F_\pi^S(q^2) = \langle \pi^+(p')|\bar{u}u + \bar{d}d|\pi^+(p)\rangle. \tag{74}$$

Indeed, on one hand side the experimental value of the pion scalar radius is known quite accurately from the analysis of $\pi-\pi$ scattering data (see Ref. [33]), which gives

$$\langle r^2\rangle_S^{\rm exp} = 0.61 \pm 0.04 \text{ fm}^2. \tag{75}$$

On the other hand side the chiral expansion of $\langle r^2\rangle_S$, calculated at NNLO in Ref. [11], reads as

$$\langle r^2\rangle_S = [\langle r^2\rangle_S]_{\rm NLO} + [\langle r^2\rangle_S]_{\rm NNLO} + \mathcal{O}(\hat{m}^2), \tag{76}$$

$$[\langle r^2\rangle_S]_{\rm NLO} = \frac{2}{F^2}\left(6\ell_4^r - 6L(\mu) - \frac{13}{2N}\right), \tag{77}$$

$$\begin{aligned}[\langle r^2\rangle_S]_{\rm NNLO} = 4\frac{x_2}{F^2}\Bigg\{&\frac{1}{N}\Bigg[88\ell_1^r + 36\ell_2^r + 5\ell_3^r - 13\ell_4^r \\ &+ \frac{145}{36}L(\mu) - \frac{23}{192} + \frac{869}{108N}\Bigg] + 31k_1 \\ &+ 17k_2 - 6k_4 + 12\ell_4^r(\ell_4^r - 2\ell_3^r) + 6r_S^r \\ &- \Delta_F\left(3\Delta_F - \frac{13}{2N}\right) - \frac{6}{N}\Delta_M\Bigg\}.\end{aligned} \tag{78}$$

It can be seen that the LEC $\bar{\ell}_4$, which also governs the NLO correction to the pion decay constant [see Eq. (60)], appears in Eq. (77).

As already stressed, the experimental value $\langle r^2\rangle_S^{\rm exp}$ is expected to be dominated by the NLO contribution (77). Using the values of the relevant LECs of the second column of Table V one gets $[\langle r^2\rangle_S]_{\rm NLO} = 0.716 \pm 0.014$ fm^2, which overestimates the experimental value (75) by almost 3 standard deviations. Thus we want to use the NNLO calculation of $\langle r^2\rangle_S$, also for consistency with the use of Eqs. (56)–(67) for the other observables. In order to do that we need to set the value of the parameter r_S^r appearing in Eq. (78). In Ref. [11] an estimate of r_S^r at the ρ-meson mass scale has been obtained using a resonance model, namely $r_S^r \approx -0.3\cdot 10^{-4}$. We have checked that using the above value or putting the parameter r_S^r equal to zero does not produce any significant difference in our chiral fits. This is not surprising since the effects of a nonvanishing value of r_S^r are expected to be relevant at large quark masses only. Thus in what follows the value $r_S^r = 0$ is assumed.

Including the experimental value $\langle r^2\rangle_S^{\rm exp}$ in the ensemble of fitted data and Eqs. (76)–(78) in the fitting procedure, we obtain the results shown in Fig. 15 with the values of the fitting parameters reported in the fourth column of Table V. Let us recall that the experimental value of the pion charge radius is not included in the fitting procedure.

Our expectation about the reduction of the uncertainties of the fitting parameters is fully confirmed. Thanks to the introduction of the experimental value $\langle r^2\rangle_S^{\rm exp}$ the value of $\bar{\ell}_4$ is determined quite accurately, and this is beneficial for reducing the uncertainties of all the other LECs (compare the third and the fourth columns of Table V).

Note that with respect to the NLO analysis the values of both the parameter B and the lattice spacing, obtained in the NNLO analysis which includes $\langle r^2\rangle_S^{\rm exp}$, change beyond the corresponding statistical errors. On the contrary the values of the LECs F, $\bar{\ell}_3$, $\bar{\ell}_4$ and $\bar{\ell}_6$ do not change significantly.

Since our data used for the curvature rely on the assumption of the monopole behavior (see Eq. (54)), we have checked that the values of the LECs, extracted by including the curvature data obtained from the cubic fit (55), change only slightly within the statistical errors with respect to the ones reported in the fourth column of Table V.

The values of the charge radius and the curvature predicted at the physical point by the chiral fit shown in Fig. 15 are $\langle r^2\rangle^{\rm phys} = 0.456 \pm 0.030$ fm^2 and $c^{\rm phys} = (5.11 \pm 0.47)\cdot 10^{-3}$ fm^4. We perform a rough estimate of the systematic errors due to finite-volume and discretization effects. First we substitute the run R_{2a} with the run R_{2b} and fit the new set of data; the changes in the central values of the chiral parameters provide an estimate of the finite-volume effects. Second, we further substitute the runs R_{2b} and R_{5a} with the runs R_{2c} and R_{5b} at the finer lattice spacing, respectively, obtaining an estimate of discretization effects. Adding all the systematic uncertainties in quadrature, our final results are

$$\langle r^2\rangle^{\rm phys} = 0.456 \pm 0.030 \pm 0.024 \text{ fm}^2, \tag{79}$$

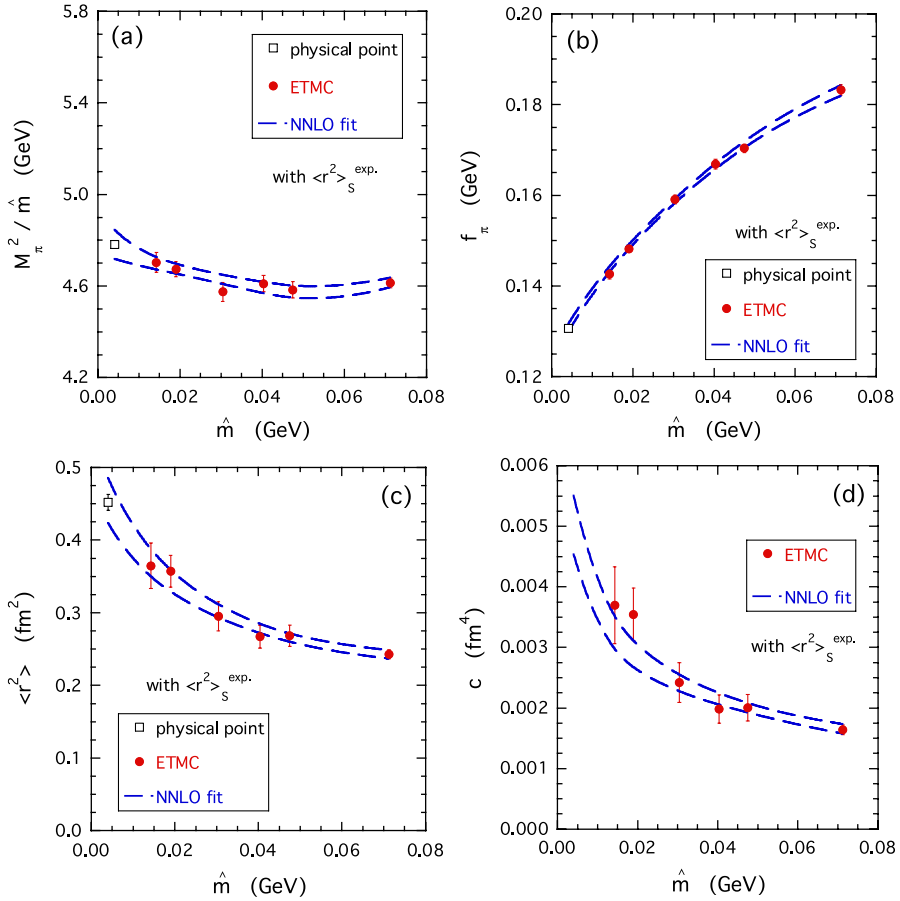

FIG. 15 (color online). As in Fig. 14, but including the experimental value of the pion scalar radius from Ref. [33] in the fitting procedure. The resulting values of the fitting parameters are listed in the fourth column of Table V.

$$c^{\rm phys} = (5.11 \pm 0.47 \pm 0.41) \cdot 10^{-3}\ {\rm fm}^4, \qquad (80)$$

where the first error is statistical and the second one systematic. We recall that the findings (79) and (80) are not completely independent, because they are based on an ensemble of fitted data which satisfy Eq. (54).

The results for the pion charge radius at the physical point obtained by various lattice collaborations performing unquenched calculations are compared in Table VII and in Fig. 16.

Our finding (79) agrees very well with the experimental value $\langle r^2\rangle^{\rm exp} = 0.452 \pm 0.011$ fm^2 [22]. It is also consistent within the errors with the results of the JLQCD ($N_f = 2$), QCDSF/UKQCD ($N_f = 2$) and UKQCD/RBC ($N_f = 2 + 1$) Collaborations, while the difference with the result of the LHP ($N_f = 2 + 1$) Collaboration is equal to ≈ 2 standard deviations.

We stress that the use of twisted BCs and the inclusion of the NNLO terms in the ChPT analyses are two important features considered in this work. Note that twisted BCs are

TABLE VII. Results for the pion charge radius extrapolated at the physical point by various lattice collaborations performing unquenched calculations. The uncertainty of the ETM result corresponds to the statistical and the systematic errors, given by Eq. (79), added in quadrature.

Collaboration	N_f	Action	$V \cdot T/a^4$	a (fm)	M_π (MeV)	$\langle r^2\rangle^{\rm phys}$ (fm^2)
ETM [this work]	2	*tl*Sym + *tmW*	$32^3 \cdot 64$	~0.09	≥ 260	0.456 ± 0.038
JLQCD [20]	2	Iw + overlap	$16^3 \cdot 32$	~0.12	≥ 290	0.404 ± 0.031
JLQCD [18]	2	plaq + Clover	$20^3 \cdot 48$	~0.09	≥ 550	0.396 ± 0.010
QCDSF/UKQCD [19]	2	plaq + Clover	$24^3 \cdot 48$	~0.08	≥ 400	0.441 ± 0.019
UKQCD/RBC [21]	2 + 1	*DWF*	$16^3 \cdot 32$	~0.12	≥ 330	0.418 ± 0.031
LHP [14]	2 + 1	Asqtad + *DWF*	$20^3 \cdot 64$	~0.12	≥ 320	0.310 ± 0.046

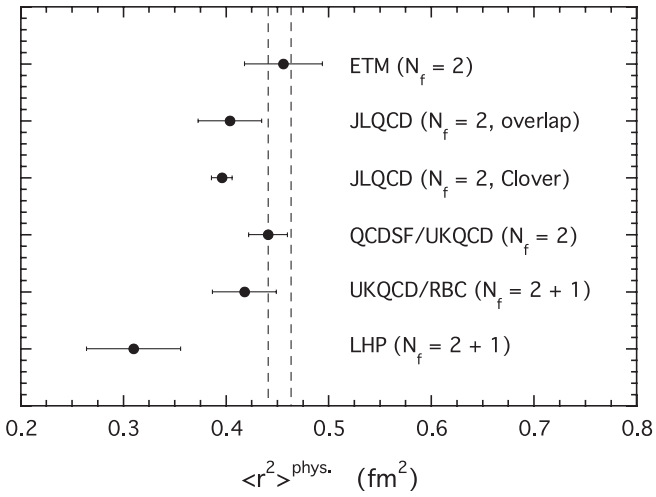

FIG. 16. Results for the pion charge radius extrapolated at the physical point by various lattice collaborations performing unquenched calculations (see Table VII). The vertical dashed lines show the experimental value $\langle r^2\rangle^{\rm exp} = 0.452 \pm 0.011$ fm^2 [22].

used only in Ref. [21], and a NNLO ChPT analysis is carried out only in Ref. [20].

The ETMC result (79) has been obtained by fitting the lattice data for values of the (squared) four-momentum transfer $Q^2 = -q^2$ up to 0.5 GeV^2 using the pole ansatz (48) or equivalently the monopole functional form

$$F_\pi^{(\rm monopole)}(Q^2) = \frac{1}{1 + \frac{\langle r^2\rangle}{6} Q^2}. \tag{81}$$

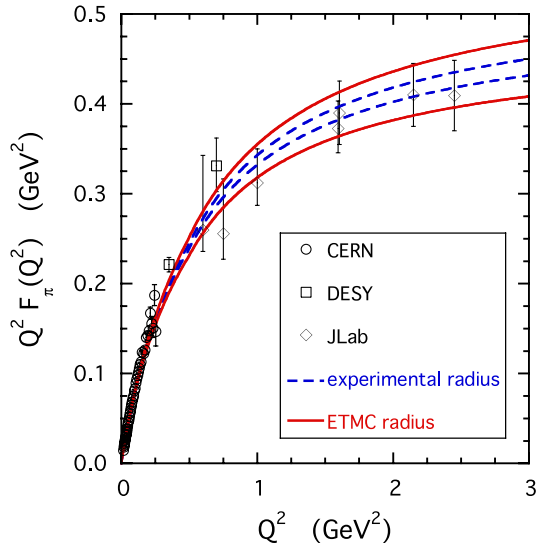

FIG. 17 (color online). Pion form factor times $Q^2 = -q^2$, $Q^2 F_\pi(Q^2)$, versus Q^2 in physical units. The dots, squares and diamonds are experimental data from Refs. [1,3–8], respectively. The dashed and solid lines correspond to the regions selected at 1σ level by the predictions of the monopole form (81) using $\langle r^2\rangle = \langle r^2\rangle^{\rm exp} = 0.452 \pm 0.011$ fm^2 [22] and $\langle r^2\rangle = \langle r^2\rangle^{\rm phys} = 0.456 \pm 0.038$ fm^2, respectively.

An interesting question is at which value of Q^2 the predictions based on Eq. (81) start to deviate from the experimental data. Recently, thanks to the CEBAF facility at JLab, the pion form factor has been measured quite accurately up to a few GeV^2. The comparison with the monopole prediction (81), using for the (squared) pion charge radius either the ETMC result (79) or its experimental value from PDG [22], is illustrated in Fig. 17.

It can clearly be seen that there is no hint of a deviation of the experimental data from the monopole ansatz up to $Q^2 \approx 2 \div 3$ GeV^2.

New experimental data up to $Q^2 \simeq 6$ GeV^2, expected to be taken after the completion of the JLab upgrade to 12 GeV [52], may shed light on the range of validity of the monopole ansatz.

C. Polynomial fit

We want to discuss briefly an alternative fit to our lattice data based on a simple polynomial form, which does not have any logarithmic term; namely

$$M_\pi^2 = 2\bar{B}\,\hat{m}\cdot[1 + C_1\hat{m} + C_2\hat{m}^2], \tag{82}$$

$$f_\pi = \bar{F}\cdot[1 + D_1\hat{m} + D_2\hat{m}^2], \tag{83}$$

$$\langle r^2\rangle = 6/(M_0 + E_1\hat{m} + E_2\hat{m}^2)^2. \tag{84}$$

The results of such a fit, applied to our lattice data having $M_\pi L \gtrsim 4$ without applying any FSE correction, are illustrated in Figs. 18 and 19.

Among the fitting parameters we obtain $2\bar{B} = 4.79 \pm 0.08$ GeV and $\bar{F} = 126 \pm 2$ MeV, while the lattice spacing turns out to be $a = 0.0889 \pm 0.0010$ fm, and the (renormalized) up/down quark mass is $\hat{m}^{\rm phys} = 3.8 \pm 0.1$ MeV.

It can clearly be seen that the quality of the polynomial fit is quite similar to the one of the ChPT fit shown in Fig. 15, and therefore we have to conclude that our lattice results do not show clear-cut evidence of chiral logs.

VI. CHIRAL FITS OF THE PION FORM FACTOR

In this section we present the ChPT analysis of our results for the pion form factor including its momentum dependence. The ChPT expansion of $F_\pi(q^2)$ has been calculated in Ref. [11] at NNLO, obtaining

$$F_\pi(q^2) = 1 + [F_\pi(q^2)]_{\text{1-loop}} + [F_\pi(q^2)]_{\text{2-loops}} + \mathcal{O}(\hat{m}^3), \tag{85}$$

$$[F_\pi(q^2)]_{\text{1-loop}} = 2x_2\left[\frac{1}{6}(w-4)\bar{J}(w) - w\left(\ell_6^r + \frac{1}{6}L(\mu) + \frac{1}{18N}\right)\right], \tag{86}$$

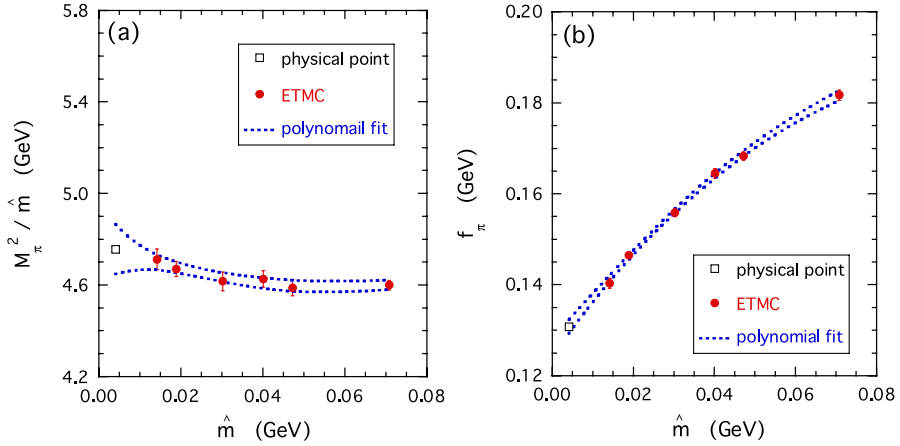

FIG. 18 (color online). The ratio $M_\pi^2/\hat{m}$ (a) and the pion decay constant (b) versus renormalized quark mass $\hat{m}$ in physical units. The dots are the ETMC results, uncorrected for FSE effects, and the squares represent the experimental value for each quantity from PDG [22]. The dotted lines correspond to the region selected at 1σ level by the polynomial fits of the squared pion mass (82) and decay constant (83).

$$[F_\pi(q^2)]_{2\text{-loops}} = 4x_2^2\Big\{P_V(w) + U_V(w) - \Delta_M \bar{J}(w) - \Delta_F\Big[\frac{1}{6}(w-4)\bar{J}(w) - w\Big(\ell_6^r + \frac{1}{6}L(\mu) + \frac{1}{18N}\Big)\Big]\Big\}, \tag{87}$$

where $w \equiv q^2/2B\hat{m}$. The polynomial part $P_V(w)$ is given by

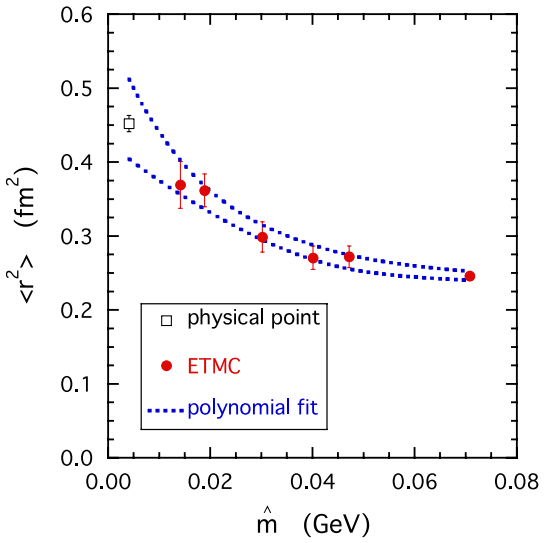

FIG. 19 (color online). The charge radius of the pion form factor versus the renormalized quark mass $\hat{m}$ in physical units. The dots are the ETMC results and the squares represent the experimental value of the pion charge radius [22], which is not included in the fitting procedure. The dotted lines correspond to the region selected at 1σ level by the polynomial fit (84).

$$P_V(w) = w\Big[-\frac{1}{2}k_1 + \frac{1}{4}k_2 - \frac{1}{12}k_4 + \frac{1}{2}k_6 + r_1^r + \frac{1}{N}\Big(\frac{23}{36}L(\mu) + \frac{5}{576} + \frac{37}{864N}\Big) - \ell_4^r\Big(2\ell_6^r + \frac{1}{9N}\Big)\Big] + w^2\Big[\frac{1}{12}k_1 - \frac{1}{24}k_2 + \frac{1}{24}k_6 + r_2^r + \frac{1}{9N}\Big(\ell_1^r - \frac{1}{2}\ell_2^r + \frac{1}{2}\ell_6^r - \frac{1}{12}L(\mu) - \frac{1}{384} - \frac{47}{192N}\Big)\Big], \tag{88}$$

while the dispersive part $U_V(w)$ reads as

$$U_V(w) = \bar{J}(w)\Big[-\frac{1}{3}w(w-4)\Big(\ell_1^r - \frac{1}{2}\ell_2^r + \frac{1}{2}\ell_6^r\Big) + \frac{1}{3}\ell_4^r(w-4) - \frac{1}{36}L(\mu)(w^2+8w-48) + \frac{1}{108N}(7w^2 - 97w + 81)\Big] + \frac{1}{9}H_1(w) + \frac{1}{9}H_2(w)\Big(\frac{1}{8}w^2 - w + 4\Big) + \frac{1}{6}H_3(w)\Big(w - \frac{1}{3}\Big) - \frac{5}{3}H_4(w), \tag{89}$$

where

$$\bar{J}(w) = zh(z) + \frac{2}{N}, \tag{90}$$

$$H_1(w) = zh^2(z), \tag{91}$$

$$H_2(w) = z^2h^2(z) - \frac{4}{N^2}, \tag{92}$$

$$H_3(w) = N\frac{z}{w}h^3(z) + \frac{\pi^2}{Nw}h(z) - \frac{\pi^2}{2N^2}, \tag{93}$$

$$H_4(w) = \frac{1}{wz}\left(\frac{1}{2}H_1(w) + \frac{1}{3}H_3(w) + \frac{1}{N}\bar{J}(w) + \frac{\pi^2-6}{12N^2}w\right), \tag{94}$$

with $z \equiv 1 - 4/w$ and

$$h(z) = \frac{1}{N\sqrt{z}}\log\frac{\sqrt{z}-1}{\sqrt{z}+1}. \tag{95}$$

Using the above formulae it is possible to test the momentum dependence of the pion form factor predicted by ChPT at NNLO. Such a dependence is analytical up to the inelastic threshold $q^2_{\rm thr} = 4M_\pi^2$. Thus, in the chiral limit, terms of the form $q^2\log(-q^2)$ appear in the pion form factor, which becomes a nonanalytic function of q^2. This is the origin of the divergency of both the charge radius and the curvature in the chiral limit [see Eqs. (62)–(67)].

It is easy to check that an expansion of Eqs. (85)–(87) in powers of q^2 leads to the result: $F_\pi(q^2) = 1 + \langle r^2\rangle q^2/6 + cq^4 + \mathcal{O}(q^6)$, with $\langle r^2\rangle$ and c given by Eqs. (62)–(67), respectively. Thus by using Eqs. (85)–(87) it is possible to take into account (at least partially) the effects of order $\mathcal{O}(q^6)$ in the momentum dependence of the pion form factor.

Note that the NNLO terms (87)–(89) do not depend upon the LECs ℓ_1^r and ℓ_2^r separately, but only through the linear combination $(\ell_1^r - \ell_2^r/2)$. Since different linear combinations of ℓ_1^r and ℓ_2^r appear in the NNLO terms of both the pion mass (58) and decay constant (61), the LECs ℓ_1^r and ℓ_2^r can be determined by a simultaneous analysis of the form factor together with the pion mass and decay constant.

As already discussed in Sec. V B, at NLO the pion form factor depends on one LEC, $\bar{\ell}_6$, which governs only the linear term in q^2. The ChPT predictions at NLO corresponding, respectively, to $\bar{\ell}_6 = 14.59 \pm 0.03$ and $\bar{\ell}_6 = 11.6 \pm 0.3$ (with $2B = 5.21 \pm 0.05$ GeV and

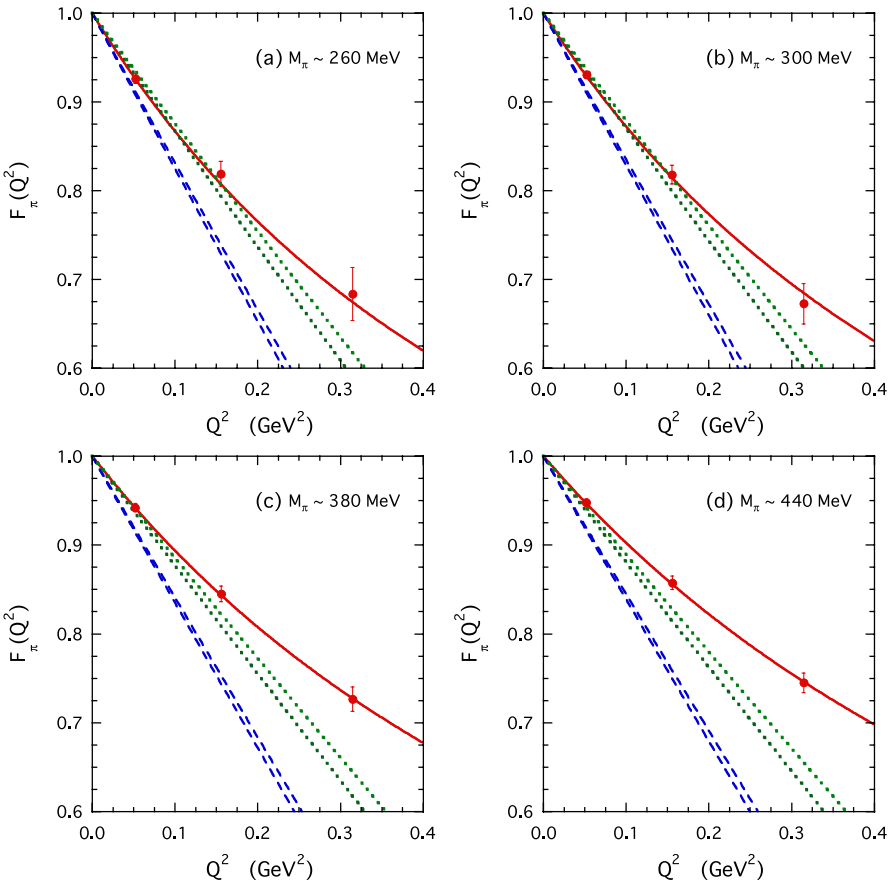

FIG. 20 (color online). Pion form factor $F_\pi(Q^2)$ versus the squared 4-momentum transfer $Q^2 \equiv -q^2$ in physical units, for the run R_1 at $M_\pi \simeq 260$ MeV (a), the run R_{2a} at $M_\pi \simeq 300$ MeV (b), the run R_3 at $M_\pi \simeq 380$ MeV (c) and the run R_4 at $M_\pi \simeq 440$ MeV (d). For the lattice spacing the value $a = 0.0861$ fm is adopted from the second column of Table V. The solid line is the pole behavior (48) with the parameter $M_{\rm pole}$ fitted to the lattice points. The dashed and dotted lines are the regions selected at 1σ level by the ChPT predictions at NLO corresponding, respectively, to $\bar{\ell}_6 = 14.59 \pm 0.03$ and $\bar{\ell}_6 = 11.6 \pm 0.3$ with $2B = 5.21 \pm 0.05$ GeV and $F = 121.7 \pm 1.1$ MeV (see text).

$F = 121.7 \pm 1.1$ MeV), reported already in Fig. 13 in the case of the pion charge radius and curvature, are shown in Fig. 20 for various values of the pion mass. We recall that the value $\bar{\ell}_6 = 14.59 \pm 0.03$ is fixed by the reproduction of the experimental charge radius, while the value $\bar{\ell}_6 = 11.6 \pm 0.3$ is obtained by fitting our lattice data of the charge radius for pion masses up to $\simeq 500$ MeV. It can be seen that:

(i) the momentum dependence predicted by ChPT at NLO is almost linear at variance with the pole behavior (48) observed in our lattice data [see also Fig. 13(b)];

(ii) using $\bar{\ell}_6 = 11.6 \pm 0.3$ the NLO approximation appears to work up to $Q^2 \equiv -q^2 \approx 0.15$ GeV^2 and for pion masses below ≈ 300 MeV. With such a value of $\bar{\ell}_6$ the NLO formula (63) yields $\langle r^2 \rangle^{\rm phys} = 0.352 \pm 0.008$ fm^2, which underestimates significantly the experimental charge radius (see Sec. V B). A slight improvement can be achieved by using directly the NLO formula (86) to fit our lattice data for the pion form factor at the lowest Q^2-value ($\simeq 0.05$ GeV^2) and for the two lowest pion masses ($M_\pi \simeq 260$ and $\simeq 300$ MeV). We obtain $\bar{\ell}_6 = 12.2 \pm 0.5$ corresponding to $\langle r^2 \rangle^{\rm phys} = 0.373 \pm 0.017$ fm^2, which still deviates from the experimental value by 4 standard deviations;

(iii) using $\bar{\ell}_6 = 14.59 \pm 0.03$, which instead reproduces the experimental value of the pion charge radius, the range of applicability of the NLO approximation reduces to values of Q^2 at least not larger than ≈ 0.03 GeV^2 and to pion masses below ≈ 300 MeV, which are not covered by our present lattice data ($Q^2 \gtrsim 0.05$ GeV^2). We notice that within the above restricted range of values of Q^2 and pion masses the deviation of the pion form factor from unity becomes smaller than a few percent, and therefore a particular attention should be paid to the statistical precision as well as to the systematic uncertainties related to cutoff and finite size effects.

From Fig. 20 it is clear that the description of our lattice data requires the inclusion of higher-order ChPT effects, which should be much larger than the finite-volume corrections and the scaling violations observed in Figs. 8 and 9 for the values of Q^2 and M_π considered in our calculations.

We have therefore performed a simultaneous NNLO fit of the lattice data of the runs R_1, R_{2a}, R_3, R_4, R_{5a} and R_6 for the quantities M_π, f_π and $F_\pi(Q^2)$, including all values of $Q^2 \equiv -q^2$ from $\simeq 0.05$ GeV^2 up to $\simeq 0.8$ GeV^2. As in the previous section, the constraint (75) on the pion scalar radius is included in the fitting procedure in order to reduce the uncertainties in the extracted values of the chiral parameters. The latter are given in the second column of Table VIII. The nice quality of the NNLO fit is illustrated in Figs. 21 and 22. The corresponding value of the pion charge radius, calculated at the physical point using Eqs. (62)–(65), is $\langle r^2 \rangle^{\rm phys} = 0.438 \pm 0.029$ fm^2, in nice agreement with the finding (79), which, we recall, is based on the use of the pole ansatz (48) that describes very well the momentum dependence of our lattice data (see Figs. 7 and 20).

The comparison of the results shown in the fourth column of Table V and those in the second column of

TABLE VIII. Values of the chiral parameters, the lattice spacing and the renormalized light-quark mass $\hat{m} = m^{\overline{\rm MS}}(2\ {\rm GeV})$ at the physical point, obtained from the simultaneous ChPT analysis of the pion mass, decay constant and form factor made at NNLO using Eqs. (56)–(61) and (85)–(87), including also the constraint (75) on the pion scalar radius. The second, third and fourth columns correspond to different Q^2-ranges of the lattice data of the form factor considered in the fitting procedure. The values of the parameters r^r_M, r^r_F, r^r_1 and r^r_2 are given at the ρ-meson mass scale. The uncertainties are statistical (bootstrap) errors only.

Parameter	$Q^2 \leq 0.8$ GeV^2	$Q^2 \leq 0.5$ GeV^2	$Q^2 \leq 0.3$ GeV^2
$2B$ (GeV)	4.89 ± 0.10	4.91 ± 0.07	4.90 ± 0.09
F (MeV)	122.6 ± 1.1	122.5 ± 0.8	122.5 ± 1.0
$\bar{\ell}_3$	3.14 ± 1.03	3.24 ± 0.53	3.19 ± 0.81
$\bar{\ell}_4$	4.37 ± 0.27	4.41 ± 0.10	4.39 ± 0.19
$\bar{\ell}_6$	15.0 ± 0.9	14.8 ± 1.1	14.8 ± 1.5
$\bar{\ell}_1$	−0.54 ± 1.01	−0.31 ± 1.12	−0.28 ± 1.91
$\bar{\ell}_2$	4.40 ± 0.78	4.29 ± 1.00	4.23 ± 1.52
$r^r_M \cdot 10^4$	−0.48 ± 0.30	−0.43 ± 0.23	−0.44 ± 0.37
$r^r_F \cdot 10^4$	0.11 ± 0.19	0.08 ± 0.10	0.08 ± 0.20
$r^r_1 \cdot 10^4$	−0.98 ± 0.12	−0.94 ± 0.13	−0.90 ± 0.14
$r^r_2 \cdot 10^4$	0.43 ± 0.03	0.46 ± 0.03	0.52 ± 0.05
a (fm)	0.0883 ± 0.0006	0.0883 ± 0.0006	0.0883 ± 0.0007
$\hat{m}^{\rm phys}$ (MeV)	3.80 ± 0.09	3.79 ± 0.07	3.79 ± 0.09
χ^2/d.o.f.	29/34	19/28	13/22

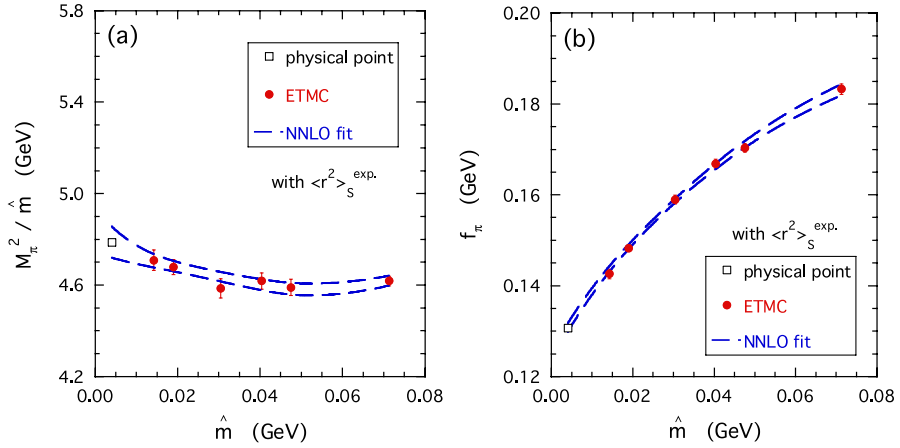

FIG. 21 (color online). The ratio of the squared pion mass to the renormalized quark mass $\hat{m}$ (a) and the pion decay constant (b) versus $\hat{m}$ in physical units. The dots are the ETMC results and the squares represent the experimental value for each quantity from Ref. [22]. The dashed lines correspond to the region selected at 1σ level by the NNLO ChPT analysis of the ETMC results for the pion mass, decay constant and e.m. form factor. The experimental value of the pion scalar radius (75) is added to the fitting procedure employing Eqs. (76)–(78). The values of the fitting parameters are listed in the second column of Table VIII.

Table VIII clearly indicates that within the statistical uncertainties the extracted values of the chiral parameters are quite stable against chiral effects of order $\mathcal{O}(q^6)$ in the pion form factor with the only exception of the parameter r_2^r, which instead exhibit a rather large variation. The latter will be included in the systematic error (see later Table IX), providing the dominant source of uncertainty for the parameter r_2^r.

We recall that, at variance with the results reported in Table V, the ones shown in Table VIII are obtained without the assumption of the pole ansatz (48) for the momentum dependence of the form factor, but using only the functional forms (85)–(89) predicted by ChPT at NNLO.

Effects from higher orders in the chiral expansion are expected to become more and more important as the value of Q^2 increases. In order to check their relevance in our

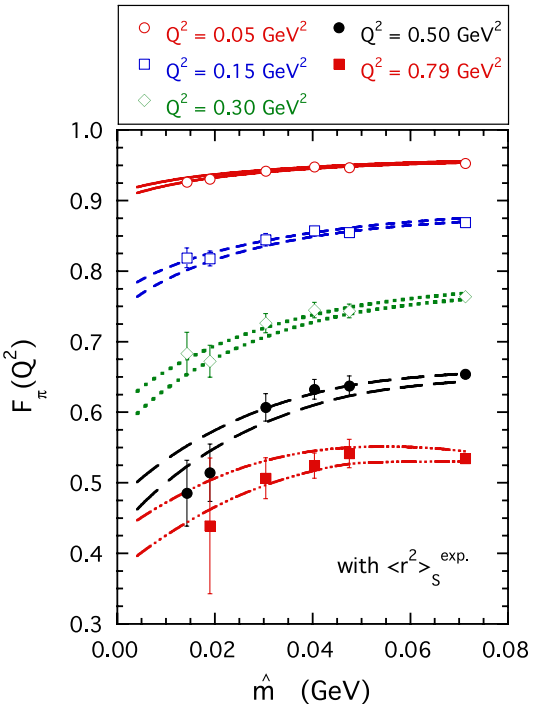

FIG. 22 (color online). ETMC results for the pion e.m. form factor versus the renormalized quark mass $\hat{m}$ at various values of $Q^2(\equiv -q^2)$. The various lines correspond to the regions selected at 1σ level by the ChPT fit at NNLO based on Eqs. (85)–(87) with the fitting parameters given in the second column of Table VIII. The experimental value of the pion scalar radius (75) is added to the fitting procedure using Eqs. (76)–(78).

TABLE IX. Values of the LECs obtained from the NNLO ChPT analyses of the previous section and compared with available estimates arising either from NNLO ChPT analyses of $\pi - \pi$ scattering data [33] or from VMD models [11]. The values of the parameters r_M^r, r_F^r, r_1^r and r_2^r are given at the ρ-meson mass scale. In the second column the first error is statistical and the second one systematic.

LEC	ETMC (NNLO) (this work)	Nonlattice estimates
$2B$ (GeV)	$4.90 \pm 0.09 \pm 0.20$	⋯
F (MeV)	$122.5 \pm 1.0 \pm 1.0$	⋯
$\bar{\ell}_1$	$-0.4 \pm 1.3 \pm 0.6$	-0.4 ± 0.6 [33]
$\bar{\ell}_2$	$4.3 \pm 1.1 \pm 0.4$	4.3 ± 0.1 [33]
$\bar{\ell}_3$	$3.2 \pm 0.8 \pm 0.2$	2.9 ± 2.4 [33]
$\bar{\ell}_4$	$4.4 \pm 0.2 \pm 0.1$	4.4 ± 0.2 [33]
$\bar{\ell}_6$	$14.9 \pm 1.2 \pm 0.7$	⋯
$r_M^r \cdot 10^4$	$-0.45 \pm 0.30 \pm 0.10$	⋯
$r_F^r \cdot 10^4$	$0.08 \pm 0.16 \pm 0.05$	⋯
$r_1^r \cdot 10^4$	$-0.94 \pm 0.13 \pm 0.10$	-2.0 [11]
$r_2^r \cdot 10^4$	$0.46 \pm 0.03 \pm 0.31$	2.1 [11]

analysis we repeat the NNLO fit by limiting the range of values of Q^2, i.e., by including only lattice data with $Q^2 \leq 0.5$ GeV^2 (see third column of Table VIII) and $Q^2 \leq 0.3$ GeV^2 (see fourth column of Table VIII). It can clearly be seen that, within the statistical precision, the extracted values of all the chiral parameters are only slightly sensitive to the Q^2-range used and therefore to higher-order effects.

Before closing this section we mention that in Refs. [24,33,34] a different definition of the LECs at NNLO is adopted, namely, the constants r_M^r and r_F^r are replaced by the constants k_M and k_F. Using the results of the second column of Table VIII we obtain $k_M = -0.6 \pm 1.6$ and $k_F = 1.2 \pm 1.5$.

VII. FINAL RESULTS FOR THE LEC'S

In this section we provide the final estimates of the LECs from the present work. Our results, including both the statistical and the systematic uncertainties, are collected in the second column of Table IX. They have been evaluated by averaging the three central values reported in Table VIII, using the quoted errors as the weights.

As in the case of the charge radius and curvature, discussed in the previous section, we estimate the systematic errors due to both finite-volume and discretization effects. First we substitute the run R_{2a} with the run R_{2b} and fit the new set of data; the changes in the central values of the chiral parameters provide an estimate of the finite-volume effects. Second, we further substitute the runs R_{2b} and R_{5a} with the runs R_{2c} and R_{5b} at the finer lattice spacing, respectively, obtaining an estimate of discretization effects. All the systematic errors, which include also the spread of the central values of Table VIII, are finally added in quadrature.

In Table IX our estimates of the chiral parameters are compared with available results from NNLO ChPT analyses of $\pi - \pi$ scattering data from Ref. [33], and with estimates obtained using VMD models in Ref. [11]. Our values for the LECs $\bar{\ell}_1$, $\bar{\ell}_2$, $\bar{\ell}_3$ and $\bar{\ell}_4$ agree nicely with those extracted in Ref. [33]. The uncertainties obtained in this work for the LEC $\bar{\ell}_4$ are quite similar to the one from Ref. [33], while $\bar{\ell}_1$ and $\bar{\ell}_2$ are determined more precisely in Ref. [33] and $\bar{\ell}_3$ in the present work.

On the contrary the estimates of the counter-terms r_1^r and r_2^r obtained in Ref. [11] adopting VMD models turn out to be much larger than our values by a factor $\approx 2 \div 3$.

The results obtained for the lattice spacing, $a = 0.0883 \pm 0.0006$ fm, and the renormalized up/down quark mass, $\hat{m}^{\rm phys} = 3.79 \pm 0.08 \pm 0.15$ MeV, are consistent within the errors with the findings of Refs. [23,50] obtained at the same value of $\beta(= 3.9)$. The values $2B = 4.90 \pm 0.09 \pm 0.20$ GeV and $F = 122.5 \pm 1.0 \pm 1.0$ MeV correspond to a light-quark condensate equal to

$$\langle q\bar{q}\rangle^{\overline{\rm MS}}(2\ {\rm GeV}) = (-264 \pm 3 \pm 5\ {\rm MeV})^3; \qquad (96)$$

TABLE X. Values of the pion form factor $F_\pi^{\rm phys}(Q^2)$, extrapolated to the physical point using for the LECs the results of Table IX, for various values of Q^2. The first error is statistical and the second one systematic.

Q^2(GeV^2)	$F_\pi^{\rm phys}(Q^2)$
0.050	$0.914 \pm 0.005 \pm 0.003$
0.148	$0.774 \pm 0.013 \pm 0.008$
0.299	$0.618 \pm 0.019 \pm 0.013$
0.503	$0.487 \pm 0.022 \pm 0.017$
0.794	$0.437 \pm 0.030 \pm 0.026$

moreover, the ratio $f_\pi^{\rm phys}/F$ is equal to

$$f_\pi^{\rm phys}/F = 1.067 \pm 0.009 \pm 0.009. \qquad (97)$$

The findings (96) and (97) are in agreement with the corresponding values obtained by the scaling analysis of Ref. [34].

Using for the LECs the values given in Table IX we have calculated the values of the pion form factor at the physical point for the various values of Q^2 considered in this work. Our results, including both statistical and systematic uncertainties, are collected in Table X and shown in Fig. 23, where they are also compared with available experimental data from Refs. [1,3–8].

It can be seen that our values are fully consistent with the experimental data in the whole range of values of Q^2 considered in this study. The agreement is particularly remarkable at low values of Q^2 ($Q^2 \lesssim 0.15$ GeV^2), where the experimental data are very precise, as well as at larger

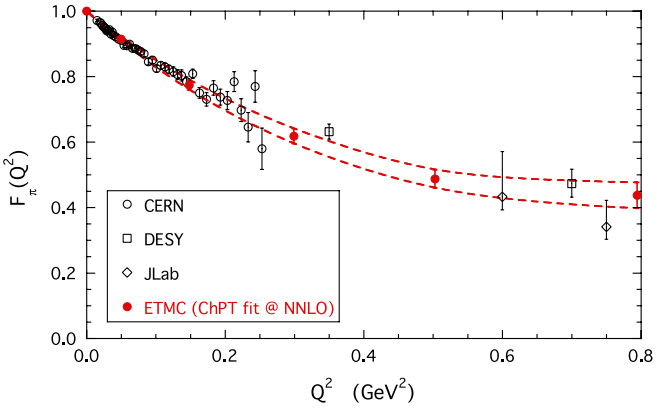

FIG. 23 (color online). Pion form factor $F_\pi(Q^2)$ versus $Q^2 = -q^2$ in physical units. The full dots are the NNLO ChPT results of Table X, obtained at the physical point using for the LECs the values given in Table IX. The uncertainties of the ETMC results, illustrated also by the dashed lines, represent the statistical and the systematic errors of Table X added in quadrature. The open dots, squares and diamonds are experimental data from Refs. [1,3–8], respectively.

values of Q^2 ($Q^2 \gtrsim 0.3$ GeV^2), where the uncertainties of our results become competitive with the experimental errors.

VIII. CONCLUSIONS

We have presented a lattice calculation of the electromagnetic form factor of the pion obtained using the tree-level Symanzik improved gauge action with two flavors of dynamical twisted Wilson quarks.

The simulated pion masses range from $\simeq 260$ to $\simeq 580$ MeV, and the lattice box sizes are chosen in order to guarantee that $M_\pi L \gtrsim 4$.

Accurate results for the form factor are obtained using all-to-all quark propagators evaluated with the stochastic procedure of Ref. [30].

The momentum dependence of the pion form factor is investigated up to values of the squared four-momentum transfer $Q^2 \simeq 0.8$ GeV^2 and, thanks to the use of twisted boundary conditions, down to $Q^2 \simeq 0.05$ GeV^2. The Q^2-dependence at the simulated pion masses is well reproduced by a single monopole ansatz with a pole mass lighter by $\approx 10\% \div 15\%$ than the lightest vector-meson mass.

Volume and discretization effects on the form factor have been directly evaluated performing simulations at different volumes and lattice spacings, and they turn out to be within the statistical errors. A more complete investigation of the scaling properties of the pion form factor, based on the study of its mass dependence at two additional values of the lattice spacing, is however desirable. The corresponding measurements are in progress.

The extrapolation of our results for the pion mass, decay constant and form factor to the physical point has been carried out using (continuum) ChPT at NNLO [11]. The extrapolated value of the (squared) pion charge radius is $\langle r^2 \rangle^{\rm phys} = 0.456 \pm 0.030_{\rm stat} \pm 0.024_{\rm syst}$ in nice agreement with the experimental result $\langle r^2 \rangle^{\rm exp} = 0.452 \pm 0.011$ fm^2 [22]. The extrapolated values of the pion form factor agree very well with the experimental data up to $Q^2 \simeq 0.8$ GeV^2 within uncertainties which become competitive with the experimental errors for $Q^2 \gtrsim 0.3$ GeV^2.

The relevant low-energy constants appearing in the chiral expansion of the pion form factor are extracted from our lattice data adding only the experimental value of the pion scalar radius [11] in the fitting procedure. We get: $\bar{\ell}_1 = -0.4 \pm 1.3 \pm 0.6$, $\bar{\ell}_2 = 4.3 \pm 1.1 \pm 0.4$, $\bar{\ell}_3 = 3.2 \pm 0.8 \pm 0.2$, $\bar{\ell}_4 = 4.4 \pm 0.2 \pm 0.1$, $\bar{\ell}_6 = 14.9 \pm 1.2 \pm 0.7$, where the first error is statistical and the second one systematic. Our findings are in nice agreement with the results of the NNLO ChPT analysis of $\pi - \pi$ scattering data of Ref. [33]. The values found for the LECs $\bar{\ell}_3$ and $\bar{\ell}_4$ are consistent with the corresponding results of the ETMC analysis of Ref. [34]. This is quite reassuring because different kinds of systematic uncertainties may affect the two analyses: the present one being a NNLO analysis limited mainly to data from a single lattice spacing, and that of Ref. [34] having two values of the lattice spacing but limited mainly to an NLO analysis.

It is the aim of our collaboration to reduce as much as possible all the uncertainties of the extracted low-energy constants in the next future. To this end, data at more values of the lattice spacing and calculations of other physical quantities, like, e.g., the pion scattering lengths, will be considered. This may allow to avoid any input from experiments obtaining a first principle computation of the low-energy constants.

In this respect a very interesting strategy is to include lattice data for the scalar form factor of the pion, because almost the same low-energy constants enter the chiral expansion of both vector and scalar form factors [11]. In this way the use of the experimental value of the pion scalar radius in the fitting procedure can be avoided. However the lattice calculation of the scalar form factor requires the evaluation of both connected and disconnected diagrams. While the former have been already calculated on the ETMC gauge configurations, a precise evaluation of the latter is in progress. The results will be reported elsewhere.

ACKNOWLEDGMENTS

We thank all the members of the ETM Collaboration for very fruitful discussions and for a very enjoyable collaboration. We gratefully acknowledge also several discussions with H. Leutwyler and G. Colangelo. The computer time for this project was made available to us by the apeNEXT systems in Rome and Zeuthen. We thank these computer centers and their staff for the invaluable technical advice and help.

APPENDIX

In Tables XI and XIIof this appendix we provide the values of the pion form factor $F_\pi(Q^2)$ obtained for all the simulations (see Table I) and for the various values of the squared four-momentum transfer $Q^2 \equiv -q^2$ considered in this work.

TABLE XI. Values of the pion form factor $F_\pi(Q^2)$ for various values of $Q^2 \equiv -q^2$ (in physical units) in the case of the runs R_1 and R_{2a} performed at $\beta = 3.9$ and at the lattice volume $V \cdot T = 32^3 \cdot 64a^4$. The uncertainties are statistical (jacknife) errors.

Q^2 (GeV^2)	R_1	R_{2a}
0.050	0.9269 (5)	0.930 (4)
0.148	0.819 (14)	0.818 (11)
0.299	0.683 (30)	0.672 (23)
0.503	0.485 (47)	0.514 (41)
0.794	0.242 (95)	0.439 (96)

TABLE XII. The same as in Table XI but for the runs R_{2b}, R_3, R_4, R_{5a} and R_6 performed at $\beta = 3.9$ and at the lattice volume $V \cdot T = 24^3 \cdot 48a^4$.

Q^2 (GeV^2)	R_{2b}	R_3	R_4	R_{5a}	R_6
0.050	0.936 (5)	0.942 (5)	0.948 (4)	0.947 (4)	0.953 (2)
0.148	0.830 (8)	0.845 (9)	0.857 (8)	0.855 (6)	0.869 (3)
0.299	0.704 (13)	0.726 (14)	0.745 (11)	0.743 (10)	0.764 (4)
0.503	0.581 (22)	0.607 (19)	0.632 (14)	0.637 (14)	0.654 (5)
0.794	0.492 (37)	0.506 (29)	0.524 (18)	0.541 (20)	0.534 (7)

TABLE XIII. The same as in Table XI but for the runs R_{2c} and R_{5b} performed at $\beta = 4.05$ and at the lattice volume $V \cdot T = 32^3 \cdot 64a^4$.

Q^2 (GeV^2)	R_{2c}	R_{5b}
0.050	0.933 (9)	0.952 (3)
0.148	0.821 (14)	0.865 (6)
0.299	0.681 (26)	0.756 (8)
0.503	0.565 (44)	0.635 (12)
0.794	0.526 (93)	0.495 (22)

[1] S. R. Amendolia *et al.* (NA7 Collaboration), Nucl. Phys. **B277**, 168 (1986).
[2] C. J. Bebek *et al.*, Phys. Rev. D **17**, 1693 (1978).
[3] H. Ackermann *et al.*, Nucl. Phys. **B137**, 294 (1978).
[4] P. Brauel *et al.*, Z. Phys. C **3**, 101 (1979).
[5] J. Volmer *et al.* (The Jefferson Lab F(pi) Collaboration), Phys. Rev. Lett. **86**, 1713 (2001).
[6] T. Horn *et al.* (Jefferson Lab F(pi)-2 Collaboration), Phys. Rev. Lett. **97**, 192001 (2006); T. Horn *et al.*, Phys. Rev. C **78**, 058201 (2008).
[7] V. Tadevosyan *et al.* (Jefferson Lab F(pi) Collaboration), Phys. Rev. C **75**, 055205 (2007).
[8] G. M. Huber *et al.*, Phys. Rev. C **78**, 045203 (2008).
[9] S. R. Amendolia *et al.*, Phys. Lett. B **138**, 454 (1984).
[10] J. Gasser and H. Leutwyler, Ann. Phys. (N.Y.) **158**, 142 (1984).
[11] J. Bijnens, G. Colangelo, and P. Talavera, J. High Energy Phys. 05 (1998) 014.
[12] G. Martinelli and C. T. Sachrajda, Nucl. Phys. **B306**, 865 (1988).
[13] T. Draper, R. M. Woloshyn, W. Wilcox, and K. F. Liu, Nucl. Phys. **B318**, 319 (1989).
[14] F. D. R. Bonnet, R. G. Edwards, G. T. Fleming, R. Lewis, and D. G. Richards (Lattice Hadron Physics Collaboration), Phys. Rev. D **72**, 054506 (2005).
[15] J. van der Heide, J. H. Koch, and E. Laermann, Phys. Rev. D **69**, 094511 (2004); J. N. Hedditch, W. Kamleh, B. G. Lasscock, D. B. Leinweber, A. G. Williams, and J. M. Zanotti, Phys. Rev. D **75**, 094504 (2007).
[16] A. M. Abdel-Rehim and R. Lewis, Phys. Rev. D **71**, 014503 (2005).
[17] S. Capitani, C. Gattringer, and C. B. Lang (Bern-Graz-Regensburg (BGR) Collaboration), Phys. Rev. D **73**, 034505 (2006).
[18] S. Hashimoto *et al.* (JLQCD Collaboration), Proc. Sci., LAT2005 (2005) 336.
[19] D. Brommel *et al.* (QCDSF/UKQCD Collaboration), Eur. Phys. J. C **51**, 335 (2007).
[20] T. Kaneko, S. Aoki, T. W. Chiu, H. Fukaya, S. Hashimoto, T. H. Hsieh, H. Matsufuru, J. Noaki, T. Onogi, E. Shintani, and N. Yamada (JLQCD and TWQCD Collaborations), arXiv:0810.2590.
[21] P. A. Boyle, J. M. Flynn, A. Juttner, C. T. Sachrajda, and J. M. Zanotti, J. High Energy Phys. 05 (2007) 016; P. A. Boyle *et al.*, J. High Energy Phys. 07 (2008) 112.
[22] C. Amsler *et al.* (Particle Data Group), Phys. Lett. B **667**, 1 (2008).
[23] Ph. Boucaud *et al.* (ETM Collaboration), Phys. Lett. B **650**, 304 (2007).
[24] Ph. Boucaud *et al.* (ETM Collaboration), Comput. Phys. Commun. **179**, 695 (2008).
[25] C. Urbach (ETM Collaboration), Proc. Sci., LATTICE2007 (2006) 022 [arXiv:0710.1517]; P. Dimopoulos, R. Frezzotti, G. Herdoiza, C. Urbach, and U. Wenger (ETM Collaboration), Proc. Sci., LAT2007 (2007) 102 [arXiv:0710.2498].
[26] R. Frezzotti, P. A. Grassi, S. Sint, and P. Weisz (Alpha Collaboration), J. High Energy Phys. 08 (2001) 058.
[27] P. Weisz, Nucl. Phys. **B212**, 1 (1983).
[28] R. Frezzotti and G. C. Rossi, J. High Energy Phys. 08 (2004) 007.
[29] S. Simula (ETM Collaboration), Proc. Sci., LATTICE2007 (2006) 371 [arXiv:0710.0097].
[30] M. Foster and C. Michael (UKQCD Collaboration), Phys. Rev. D **59**, 094509 (1999); C. McNeile and C. Michael (UKQCD Collaboration), Phys. Rev. D **73**, 074506 (2006).
[31] P. F. Bedaque, Phys. Lett. B **593**, 82 (2004).
[32] G. M. de Divitiis, R. Petronzio, and N. Tantalo, Phys. Lett. B **595**, 408 (2004).
[33] G. Colangelo, J. Gasser, and H. Leutwyler, Nucl. Phys. **B603**, 125 (2001).
[34] P. Dimopoulos, R. Frezzotti, G. Herdoiza, K. Jansen, C. Michael, and C. Urbach (ETM Collaboration), arXiv:0810.2873.
[35] D. Guadagnoli, F. Mescia, and S. Simula, Phys. Rev. D **73**, 114504 (2006).

[36] C. T. Sachrajda and G. Villadoro, Phys. Lett. B **609**, 73 (2005); P. F. Bedaque and J. W. Chen, Phys. Lett. B **616**, 208 (2005); J. M. Flynn, A. Juttner, and C. T. Sachrajda (UKQCD Collaboration), Phys. Lett. B **632**, 313 (2006).
[37] W. Wilcox, hep-lat/9911013.
[38] J. Foley, K. Jimmy Juge, A. O'Cais, M. Peardon, S. M. Ryan, and J. I. Skullerud, Comput. Phys. Commun. **172**, 145 (2005).
[39] K. Jansen, C. Michael, and C. Urbach (ETM Collaboration), Eur. Phys. J. C **58**, 261 (2008).
[40] P. A. Boyle, A. Juttner, C. Kelly, and R. D. Kenway, J. High Energy Phys. 08 (2008) 086.
[41] P. Dimopoulos, R. Frezzotti, G. Herdoiza, A. Vladikas, V. Lubicz, S. Simula, and M. Papinutto (ETM Collaboration), Proc. Sci., LATTICE2007 (2006) 241 [arXiv:0710.0975].
[42] F. J. Jiang and B. C. Tiburzi, Phys. Lett. B **645**, 314 (2007).
[43] P. Dimopoulos, C. McNeile, C. Michael, S. Simula, and C. Urbach (ETM Collaboration), arXiv:0810.1220; C. Michael and C. Urbach (ETM Collaboration), Proc. Sci., LAT2007 (2007) 122 [arXiv:0709.4564].
[44] J. Gasser and H. Leutwyler, Phys. Lett. B **184**, 83 (1987).
[45] G. Colangelo, S. Durr, and C. Haefeli, Nucl. Phys. **B721**, 136 (2005).
[46] G. Colangelo and C. Haefeli, Nucl. Phys. **B744**, 14 (2006).
[47] B. Borasoy and R. Lewis, Phys. Rev. D **71**, 014033 (2005); T. B. Bunton, F. J. Jiang, and B. C. Tiburzi, Phys. Rev. D **74**, 034514 (2006); **74**, 099902(E) (2006).
[48] F. J. Jiang and B. C. Tiburzi, Phys. Rev. D **78**, 037501 (2008).
[49] C. Aubin *et al.* (HPQCD, MILC and UKQCD Collaborations), Phys. Rev. D **70**, 031504 (2004).
[50] B. Blossier *et al.* (European Twisted Mass Collaboration), J. High Energy Phys. 04 (2008) 020.
[51] K. G. Chetyrkin and A. Retey, Nucl. Phys. **B583**, 3 (2000).
[52] G. M. Huber and D. Gaskell (spokepersons), JLab proposal PR12-06-101.